Late Pleistocene slip rate of the central Haiyuan fault constrained from OSL, 14 C, and cosmogenic isotope dating and high resolution topography

Yanxiu Shao, Jing Liu-Zeng, Jérôme van Der Woerd, Yann Klinger, Michael E Oskin, Jinyu Zhang, Peng Wang, Pengtao Wang, Wei Wang, Wenqian Yao

Late Pleistocene slip rate of the central Haiyuan fault constrained from OSL, ^{14}C, and cosmogenic isotope dating and high resolution topography

Yanxiu Shao[1,2,3*], Jing Liu-Zeng[1], Jerome Van der Woerd[4*], Yann Klinger[3], Michael E. Oskin[5], Jinyu Zhang[1], Peng Wang[1], Pengtao Wang[2], Wei Wang[1], Wenqian Yao[1]

[1]Institute of Geology, China Earthquake Administration, Beijing, 100029 China

[2]Lanzhou Institute of Seismology, China Earthquake Administration, Lanzhou, 730000 China

[3]Université de Paris, Institut de Physique du globe de Paris, CNRS, F-75005 Paris, France

[4]Institut de Physique du Globe de Strasbourg UMR 7516 CNRS Université de Strasbourg, 5 rue René Descartes, 67084 Strasbourg Cedex, France

[5]Department of Earth and Planetary Sciences, University of California, Davis, California 95616, USA

Y. SHAO: shaoyx@geoidea.org

J. Van der Woerd: jerome.vanderwoerd@unistra.fr

ABSTRACT: The Haiyuan fault is a major left-lateral active fault of the India-Asia collision zone. While the 1000 km-long fault between Hala Lake in the west to Liupan Shan in the east accommodates eastward displacement of northeast Tibet relative to the Gobi-Alashan to the north, the amount of slip accumulated and its slip-rate remain debated. We revisit the site of Daqing (or Sangedun at 102.7°E in Gaudemer et al., 1995), to better constrain the long-term slip-rate of the Haiyuan fault in its central part. We used terrestrial LiDAR to build a high-resolution DEM and Unmanned Aerial Vehicle to build an aerial photomosaic with ~0.1 m resolution to survey the offset terraces, their geomorphology and the fault trace. We refine the geomorphological interpretation of the site, measure riser offsets and determine their relation to terrace formation. The well constrained age of the highest terrace T3 at 13.7 ± 1.5 ka determined from the combination of surface and sub-surface OSL, ^{14}C, and terrestrial in situ ^{10}Be cosmogenic nuclide dating, associated with the maximum lower terrace riser offset of 88 m yield a minimum slip-rate of 6.4±1.2 mm/yr over the late Pleistocene. The age of the intermediate terrace (T2) is bracketed between 8.0 ka (^{14}C) and 12 ka (^{10}Be). The ages and vertical offsets of the 2 highest terraces is used to infer the age of T2' offset vertically 5-7 m at 5.4±1 ka. Its 29±2 m offset is consistent with a rate of 6.5 mm/yr. Given the vertical offset youngest terrace T1 of 1.3±0.2 m its age is estimated at 1.2±0.2 ka in agreement with the youngest surface exposure age. Overall, a slip rate of 5-8 mm/yr fits all offset and age data at the Daqing site. The smallest offset of a gully incised into T1 of 6.0±0.5 m is potentially associated with the most recent slip event that occurred in the last millennia.

Keywords: Haiyuan fault, northern Tibetan plateau, slip rate, LiDAR, cosmogenic nuclide dating

INTRODUCTION

How strain is distributed in the Tibetan-Himalayan orogen is important to understand how continental orogens deform (Tapponnier and Molnar, 1977; England and Molnar, 1997). The Haiyuan left-lateral strike-slip fault, whose eastern part ruptured in 1920 for a length of about 220 km (Deng et al., 1984), is a major strike slip fault at the northeastern margin of the Tibetan Plateau. This fault plays an important role in accommodating eastward extrusion of the northern Tibet plateau relative to the Gobi-Alashan to the north (Tapponnier and Molnar, 1977; Burchfiel et al., 1991; Gaudemer et al., 1995; Tapponnier et al., 2001a).

Overall decadal geodetic and millennial geological recent slip-rate studies mostly agree to a rate of 4-10 mm/yr, implying that the Haiyuam fault is the major active fault at the rim of Tibet at this longitude (Li et al., 2009; Daout et al., 2016; Jiang et al., 2017). However, higher slip rates have been documented (Gaudemer et al., 1995; Zhang et al., 1988; Lasserre et al., 1999, 2002). Because it has been suggested that the fault slip rate might vary over time., thus, it is valuable to find multiple slip-rate constraints at a single site to constrain possible temporal slip-rate variations (e.g., Sieh and Jahns, 1981; van der Woerd et al., 1998, 2002; Lasserre et al., 1999; Li et al., 2009; Jiang et al., 2017; Mattrau et al., 2019).

Terrace risers have commonly been used as markers of fault displacement to constrain slip rates along strike slip faults (e.g., Lensen, 1968; Weldon & Sieh, 1985; Berryman et al., 1990; Knuepfer, 1992; Van der Woerd et al., 1998, 2002; McGill et al., 2013). However, terrace risers can be seldom directly dated. One may infer displacement started to be recorded at the time of upper terrace abandonment or upon abandonment of the lower terrace (Van der Woerd et al., 2002; Mériaux et al., 2004, 2005; Cowgill, 2007; Zhang et al., 2007). In general, upper terrace age yields a minimum slip rate, while the lower terrace age a maximum slip rate. Ideally, when

terrace ages are not too different a combination of upper and lower age constraints may be used to bracket the riser age (Mériaux et al., 2005; Cowgill, 2007).

The precision of a late Quaternary slip rate depends upon displacement accumulation and its uncertainty as well as the reliability of the corresponding dating (Cowgill et al., 2007, 2009; Gold et al., 2009; Le Béon et al., 2012; Sieh, 1981; Van der Woerd et al., 1998, 2006; Weldon & Sieh, 1984; Zhang et al., 2007). Across the Qilian Shan-Hexi Corridor, loess covers late Quaternary surface broadly. Researchers have often used optically stimulated luminescence (OSL) or radiocarbon ages of materials collected within the basal loess to date the end of terrace emplacement (e.g. Li et al., 2009; Jiang et al., 2017; Liu et al., 2018). Several studies indicate that loess deposition started just prior to the Holocene in this area (~13-10 ka) (Küstera et al., 2006; Stokesa et al., 2003). Thus, loess deposition age is a minimum age for terraces formed before the Holocene. Because terraces capped by loess are usually formed of coarse gravels, if one could correct for the shielding effect due to loess, in situ cosmogenic nuclides should be an optimal dating method, ideally complemented by OSL and ^{14}C dating of loess capping materials (e.g., Perrineau et al., 2011; Hetzel et al., 2004; Hetzel, 2013).

High-resolution topographic data make it possible to image subtle landforms and deformation features due to active tectonics, and to make reproducible and precise measurements, improving understanding of rupture history and slip along faults (e.g. Zielke et al., 2010, 2015). Satellite or aerial photography offers two-dimensional imagery which is often used to trace fault line and look for offset markers (e.g., Tapponnier and Molnar, 1977; Peltzer et al., 1989; Meyer et al., 1998; Lasserre et al., 1999; Klinger et al., 2011; Middleton et al., 2016). Studies have applied Airborne Laser Scanning (ALS) data to map fault-zone features (e.g., Hudnut et al., 2002; Oskin et al., 2007; Arrowsmith and Zielke, 2009; Liu-Zeng et al., 2013), to survey coseismic surface ruptures (Oskin et al., 2012; Clark et al., 2017; Langridge et al., 2018) or to determine paleo-earthquake slip distributions (Zielke et al. 2010, 2012;

Thackray et al., 2013; Chen et al., 2015). Recently, this technique has also been used to measure the most recent rupture traces along the eastern Haiyuan fault (Chen et al., 2014, 2018; Ren et al., 2015).

Based on new imagery and field investigation, we revisit the Daqing site (also named Sangedun site in the study of Gaudemer et al., 1995), a location with multiple marker offsets, to reassess the slip rate of the Haiyuan Fault. We constrain the slip rate at this site with new offset measurements and a combination of absolute age dating approaches.

GEOLOGIC SETTING

The Haiyuan fault extends for ~1000 km from Hala Hu within the Qilian Shan in the west to the Liupan Shan in the east (e.g., Deng et al.1984; Tapponnier and Molnar, 1977; Deng et al.1984; Burchfiel et al., 1989; Gaudemer et al., 1995; Lasserre et al., 1999; Zhang et al., 1988a, b). Thermochronological data indicate that the Haiyuan fault initiated along its western section, then perhaps propagated eastward to the Liupan Shan area (Zheng et al., 2006; Duvall et al., 2013). The fault is characterized by left-lateral strike slip with oblique-slip components along some strands. Six major sections are distinguished, which are separated by left step-overs or branches. These sections, from west to east, are Halahu, Lenglongling, Jinqiang He, Maomao Shan, Haiyuan, and Liupan Shan sections (sections 1 to 6, respectively, in Figure 1). The Gulang-Zhongwei fault branches off the Haiyuan fault near the junction of Lenglongling and Jinqiang He sections, and turns back towards the Haiyuan fault east of 106ºE. Large historical earthquakes, such as 1709 Zhongwei M7.5, 1920 Haiyuan Mw7.8-8.3 and Gulang 1927 M8.0 earthquakes, ruptured these two faults, which raises concern about seismic hazard on the faults.

Numerous field studies along the Haiyuan fault have been carried out during the last 30 years. For instance, paleoseismic investigations along the Haiyuan (e.g. Zhang et al., 1988; Ran et al., 1997; Xiang et al., 1998; Min et al., 2001; Liu-Zeng et al.,

2015) and Maomao Shan (e.g. Yuan et al., 1998; Liu-Zeng et al., 2007) sections show that earthquakes can rupture single or several sections together, and cluster temporally (Zhang et al., 2003). Magnitude 6 to 7 earthquakes were also evidenced in trenches with high-resolution deposition sequences (Liu-Zeng et al., 2015). Six events were revealed on the Lenglongling section, and the most recent event may be the Gulang M8.0 earthquake in 1927 (Guo et al., 2019).

Geological slip rates determined along the Haiyuan fault differ greatly between different studies, from a few mm/yr to more than 1 cm/yr (Table S1), which are due to different dating methods and slip reconstruction models. Lasserre et al. (2002) estimated the slip rate of the Lenglongling segment to be 19 ± 5 mm/yr according to the study of a dated offset moraine. However, He et al. (2000) argued for a lower slip rate along the Lenglongling segment of 3.3 ~ 4.1 mm/yr during the late Quaternary, although without dating constraints. Recently, Jiang et al. (2017) investigated the eastern section of the Lenglongling segment and estimated a left-lateral slip rate of 6.6 ± 0.3 mm/yr during the Holocene by ^{14}C and OSL dating. Lasserre et al. (1999) determined a slip rate of 12 ± 4 mm/yr along Maomao Shan segment. While Yuan et al. (1998) estimated lower slip rates on the Maomao Shan segment to be 4.1-5.4 mm/yr. Yao et al. (2019) recently reassessed the estimation of Lasserre et al. (1999) with a slip rate for the Haiyuan fault between 5 and 8.9 mm/yr over the late Pleistocene - Holocene. Liu et al. (2018) also estimate a low slip rate of 4.3 ± 0.16 mm/yr from four offset terraces on the Laohu Shan segment. The Haiyuan segment, which ruptured in 1920 during a magnitude Ms8.0 (Richter, 1958), was assigned a slip rate of 8 ± 2 mm/yr by Zhang et al. (1988). Li et al. (2009) updated this value to ~4.5±1 mm/yr by dating offset alluvial terraces. Matrau et al. (2019) constrained a minimum slip rate of 3.2 ± 0.2 mm/yr along the main strand of the Hasi Shan restraining bend along the western section of the 1920 Haiyuan earthquake rupture. Further east, the slip rate decreases to about 1~3 mm/yr along the Liupanshan segment (Xiang et al., 1999).

159 The Jinqiang He section (3) (named after the name of the Jinqiang river) and the
160 Maomao Shan section (4) are linked across a 6 km left step by a N45°E-striking and
161 east dipping normal fault, which bounds the Tianzhu half-graben or pull-apart basin to
162 the west (Gaudemer et al., 1995; Figure 2). There is no evidence of large earthquake
163 during at least the past eight centuries along these two fault sections, which are
164 considered as "the Tianzhu seismic gap" (Gaudemer et al., 1995; Liu-Zeng et al.,
165 2007). The fault offsets alluvial fans and ridges along the northern side of the Jinqiang
166 He valley, then steps to the north at the Tianzhu pull-apart basin with mostly a large
167 normal component before veering eastward to resume a N110°E strike. The southern
168 rim of the Tianzhu basin is limited by a minor fault strand (Figure 2) with no evidence
169 of faulting during the Holocene.
170 The site of Daqing (or Sangedun site in Gaudemer et al., 1995; Tapponnier et al.,
171 2001b) is located along the eastern part of the Jinqiang section, north of the Daqing
172 village (Figure 1). A stream that flows down from a high catchment (elevation >4000
173 m asl) and perpendicular to the main fault has abandoned a set of 3 main terrace
174 levels along its west bank (Figure 2). These terraces are cut and offset by the fault.
175 Based on fieldwork, aerial-photo interpretation, and topographic leveling with a
176 theodolite, Gaudemer et al. (1995) determined the horizontal and vertical offsets of
177 the three main terrace levels to be 143 m, 89 m, 35 m and 18 m, 11 m, and 4 m,
178 respectively. Assigning an abandonment age of 13.5±2ka to the highest terrace based
179 on the assumption that it was deposited and abandoned during the wetter and warmer
180 period following the last late glacial maximum, they proposed a slip-rate of 11±4
181 mm/yr. However, more recent slip rates determined in a range of 100 km from the
182 Daqing site, respectively westward and eastward along the Jinqiang and Maomoshan
183 sections, are much lower and range from 1.8 to 4.8 mm/yr based on soil sequence
184 comparison (Yuan et al., 1998). The slip rate determined for a similar period of time
185 (10-25 ka) by Yao et al. (2019) is 5 to 9 mm/yr at Songshan (a site located at a

distance of ~80 km to the east). Thus, the slip-rate of the central Haiyuan fault along the Jinqiang He section remains arguable.

LEVELING AND GEOCHRONOLOGY METHODS

Terrestrial LiDAR (TLS) was used to generate a detailed scan of the landscape of the Daqing site. We used a Riegl VZ-1000, with an effective scan range of ~1400 m and a precision of ~5 mm. Three successive scans were needed to cover all the studied area. A Trimble real-time kinematic (RTK) Global Position system (GPS) surveyed each scanning base position and elevation. These positions were used to register the different point cloud datasets together. Even though TLS scans the landscape with a rate of more than one hundred thousand points per second, some places may remain hidden due to topographic roughness. In addition to TLS, we used a small drone equipped with a fixed focus camera to capture aerial imagery vertically and obliquely to generate an ortho-photo mosaic of the site by structure from motion techniques (Figures 3 and 4). We projected the DEM derived from points cloud of TLS in the same coordinates of the ortho-photo.

At the Daqing site, large boulders armor the surface of the terraces, some of them are partially buried into the subsurface. Rock samples for terrestrial cosmogenic nuclide dating were collected from the top of blocks using chisel and hammer (Figure 4 and 5). In addition, a pit was dug into the highest terrace (T3) for sub-surface sampling (Figure 6). The upper 1.1 m of the profile consists of 80 cm thick dark brown to black soil topping a 30 cm silty (loess) layer mixed with gravels. From these upper layers we sampled 2 radiocarbon samples at 62 and 77 cm depths, and 2 OSL samples at 82 and 104 cm depths (Tables 1 and 2). In the lower conglomeratic part of the profile, we collected 8 samples of amalgamated gravels and pebbles down to 3 m depth for cosmogenic isotope dating. All sample locations were recorded using a portable GPS and elevations was adjusted with the topography data from the TLS (Figure 5).

Radiocarbon samples were analyzed by Beta Analytic with accelerator mass spectrometry (AMS) and calibrated using Calib 7.1 (Stuiver et al., 1993) (Table 1). The two OSL samples were processed and analyzed following Aitken (1998) and Lu et al. (2007). Coarse-grained quartz was purified from samples through chemical separation using 30% H2O2, 10% HCl, and 40% HF, and magnetic separation. The ratio of Infra-red Stimulated Luminescence (IRSL) to Blue Light Stimulated Luminescence (BLSL) has been checked to be lower than 45% to make sure the quartz is clean. A Risø TL/OSL-DA-20 reader was used for irradiation, heating and luminescence measurements (Table 2 and Figure 7). All dose rates were calculated by the central age model (Galbraith et al., 2012). The samples analyzed for ^{10}Be cosmogenic nuclide were pre-processed at the Key Laboratory of Crustal Dynamics, China Earthquake Administration. We crushed the gravels and pebbles, purified the 250-500 μm fraction with acid leaches to obtain pure quartz, then dissolved about 30 g of quartz to which 0.25 mg of Beryllium-9 standard solution was added with hydrofluoric acid. We isolated beryllium hydroxide (BeOH2) using cation exchange chromatography, which was then heated to 700°C to form beryllium oxide (BeO). Final targets were prepared at the Cosmogenic isotope Laboratory of Institut de Physique du Globe de Strasbourg (CNRS, University of Strasbourg) and sent to the ASTER-AMS facility of Centre Européen de Recherche et d'Enseignement des Géosciences de l'Environnement (Aix-en-Provence, France) for measurement (Table 3).

RESULTS

Accumulated slip determination

Combining the DEM with a resolution of ~0.1 m computed from point clouds acquired by TLS, the kinematic GPS topographic profiles, and the aerial orthophoto mosaic acquired by UAV, we produce a geomorphic map of the Daqing site (Figures 3 and 4). Overall, our mapping and leveling are consistent with previous

242 interpretation of the site by Gaudemer et al. (1995). Three main terrace levels are
243 abandoned and preserved on the right bank of the Daqing stream. These are offset
244 both horizontally and vertically due to oblique fault slip. The trace of the main
245 Haiyuan fault can be clearly followed along the steepest part of the topographic scarp
246 trending N110ºE. The fault trace, as noted by Gaudemer et al. (1995), is marked by
247 roughly aligned large blocks visible in the active stream bed that are clearly visible on
248 the aerial photo (Figure 3).

249 The terrace levels are well defined and separated by steeply sloping risers
250 (Figure 4). The terrace surfaces slope 14º to 8º from oldest to youngest (Figures 4 and
251 8) reflecting progressive incision and slope lowering of fan shape deposits (Figure 8).
252 The highest terrace level T3 is present to the west and cut by the fault visible at the
253 base of a 15 m-high scarp. The intermediate terrace level is subdivided into older
254 higher standing ridges (T2) dotted with large outcropping blocks and incised by
255 channels at a lower level (T2'). Another sub-level terrace T2'' is locally distinguished
256 upstream. The lowest terrace level T1 stands a few meters above the active river bed.
257 At places, gullying and riser-slope instabilities have added some disturbance to the
258 overall simple geomorphological setting. The height and width of the fault scarp are
259 larger on the older terraces than the younger terraces, due to additional accumulated
260 deformation and progressive degradation of the steep fault scarp (Figures 4) (e.g.,
261 Tapponnier et al., 1990; Zinke et al., 2015). In addition, due to relative vertical
262 motion on the fault, terrace separation and riser heights upstream are much larger than
263 downstream with no marked changes in average slopes of the terraces (Figure 8).

264 Because of lateral stream erosion and local degradation of terrace risers, terrace
265 edges are not linear features, especially upstream of the fault, which makes it difficult
266 to reconstruct their geometry prior of being offset. Downstream risers T3/T2' and
267 T2/T1 are curved near the fault trace (Figure 4), which suggests that displacement of
268 the risers started to accumulate before the lower terrace levels were completely
269 abandoned.

We bracket higher and lower displacement values by fitting far-field riser edges (more than 200 meters-long away from fault trace) and near-field riser edges (few tens of meters long from fault trace) across the fault. Risers slope toward the river bed, so offsets related to riser top and bottom are also specified, especially offsets of curved risers nearby fault trace (Figure 9). All measurements are shown in Table 4. It is worth pointing out that the far field displacements of riser tops (D#u) may be related to the abandonment of the adjacent upper terrace, while near-field displacements (e.g. d3u, d3l, d2u, d2l) (Figure 9F) are more closely related to the adjacent lower terrace and regarded as a minimal offset value for the upper adjacent terrace (e.g., Gold et al., 2011a).

For terrace riser T3/T2', the crest of the upstream riser may be fit in two ways. First option is that piercing line fits tangentially two convex bumps close to the fault. The second option is a piercing line fit to the concave curve between those two convex bumps, similar to Gaudemer et al. (1995). Downstream, the top edge of the riser is smoothed near the fault zone because of erosion when T2 or T2' were active. Therefore, we locate the piercing line away from this erosion area. Bottom piercing lines of riser T3/T2' are almost parallel to the top. Correlating piercing riser crest lines from upstream and downstream of fault, the displacement of the crest is 82 ±3 to 94±3 m, or 88±9 m. 94±3 m is similar to the measurement of 101.5 m obtained by Gaudemer et al. (1995). Piercing lines at base of riser constrain an offset of 72±3 m. Considering the different possibilities, displacement of T3/T2' ranges from 72±3 to 88±9 m. The near field displacements by fitting bent riser crest (d3u) and bottom (d3l) are similar 25±2 - 28±2 m or 26±2 m (Figure 4, Table 4).

Riser T2/T1 is almost linear with exception of a small bump outward upstream and erosion near the fault. We neglect this minor curve, which does not affect much the maximum slip estimate. Downstream, piercing lines along riser crest and bottom are not exactly parallel because of diffusion of the riser. The cumulated slip of riser T2/T1 ranges from 27±2 m to 35±2 m or 31 ± 4 m. This value is similar to the offset

298 of the western edge of T2 (or riser T2/T2') of 29±2 m. The near field displacement of
299 the bent riser T2/T1 along the fault is 6.5 ± 1 m (d2u and d2l, Figure 4, Table 4).
300 Riser T1/T0 does not preserve lateral slip, even though T1 and T0 were likely
301 ruptured in the past (Figures 4 and 10). A small stream incising the inner T1 surface,
302 however, was offset by 6.0 ± 0.5 m (Figure 10A), which is similar with d2u and d2l.
303 Total displacements of terraces, however, are larger than the offsets of lower
304 risers and smaller than upper risers because of probable lateral erosion when lower
305 terraces were active. Therefore, 88±9 m can be defined as the lower bound for offset
306 of T3, the offset of T2 is between 72±3 m and 35±2, the horizontal offset of T1 is 6.5
307 ± 1 m. For T2', the offsets of its west and east edges are 28±2 m and 29±2 m
308 respectively (Figure 4). Thus, its offset is well constrained to be 29±2 m.
309 In addition to left lateral slip, the Haiyuan fault exhibits a vertical component of
310 slip at this site. We used a dGPS survey to measure the throw along the riser crests to
311 take into account the apparent vertical offset due to displacement of obliquely sloping
312 terrace surfaces (e.g., Rodgers and Little, 2006; Chevalier et al., 2016). Therefore,
313 scarp height of 15 ± 2 m (Sc3) across T3 as measured from the profiles (Figure 8)
314 may be larger than the real throw. The scarp height measured along the swath profile
315 in the middle of terrace T3 (19 ± 2 m) is even larger than on the edge (15 ± 2 m)
316 (Figure 4 and 7) since the terrace slopes toward the west (see details in Gaudemer et
317 al., 1995). The maximum slope direction of terrace T3 on both side of the fault makes
318 an angle of ~4.2° with a perpendicular to the fault trace. Taking this angle and
319 assuming 94±3 m is the total offset of T3, the measured vertical slip of 19 ± 2 m (Vi)
320 is corrected to 13±2 m (Vr) (e.g., Gaudemer et al., 1995; Figure 8), which is close to
321 the value found on the terrace edge (15±2 m). Maximum slopes of terrace T2 across
322 the fault are similar and perpendicular to fault trace, so that no correction is needed
323 for T2 and its vertical throw is 10 ± 1 m (Sc2) (Figure 8).
324 The slopes of T1 are similar upstream and downstream, both from dGPS
325 measurements and a swath profile through the LiDAR DEM. The height of the fault

scarp across T1 is 1.3±0.2 m (Figure 8). This value is smaller than the vertical displacement of ~4.1 m across T1 estimated by Gaudemer et al. (1995).

Five topographic profiles parallel to the Haiyuan fault (Figures 3 and 8) illustrate how riser heights change across the fault scarp (Table 4). Riser T3/T2' is 15-19 m high upstream, but less than 2 m downstream. Height of riser T2/T1 is also larger upstream (12-13 m) than downstream (~7.5 m). T1 is ~6 m high above the active bed upstream, and only ~2.5 m high downstream.

Terrace ages

To constrain the age of abandonment of T3 we dug a 3 m-deep pit in the downstream tread of terrace T3 (Figure 3). The upper 1.1 m of the profile exhibits a 30 cm sandy-loessic layer overlain by an 80 cm-thick black silty soil, which developed from the loess including some coarse sand. Below 1.1 m depth, the profile penetrates the conglomeratic terrace deposit made of blocks, cobbles, gravels and sand. Two OSL samples from the loess layer yield ages of 12.2 and 8.7 ka, in stratigraphic order (Figure 4 and Table 2). Two radiocarbon samples from the lower part of the soil give ages of 7.7 and 7.6 ka, also in stratigraphic order (Figure 4, Table 2). Whether the loessic layer is of eolian origin or reworked loess in over bank deposits cannot be confirmed. In any case, the 1.1 m top of the terrace indicates deposits of low energy incompatible with the presence of an active stream and thus indicates that the underlying conglomerate has been abandoned prior to deposition of these upper layers, i.e., prior to 12.2 ka. To better constrain the age of abandonment of the terrace, we modeled the Berylium-10 concentration with depth for 8 amalgamated gravel-pebble samples collected in the conglomeratic terrace deposit (Table 3). To take into account the shielding effect of the loess and soil we propose 3 end-member models (Figure 11A, B, C). The first one (model 1) is a maximum shielding or maximum age model, where despite some knowledge of the loess and soil ages, we consider that loess and soil were deposited immediately after the abandonment of conglomerate T3 was abandoned. Considering the respective density for sandy-loess

of 2.0 and soil of 1.2, the best fit of the ^{10}Be data is obtained with an exposure age of 21.6 ± 4.6 ka ($t_{1\text{-}1}$) (Figure 11). Clearly, given the age of the lowermost OSL sample of 12.2 ka, this age is not realistic and is too old. A second model (model 2) takes into account the oldest ages of the sandy-loess and soil deposit as the moment when these layers were deposited. This model has thus 3 exposure phases, a first one corresponding to the abandonment of the conglomerate without shielding (between $t_{2\text{-}1}$ and $t_{2\text{-}2}$), a second one, with 30 cm of sandy-loess shielding starting at 12.2 ka ($t_{2\text{-}2}$), and a third one, with the additional 80 cm of soil shielding starting at 7.7 ka ($t_{2\text{-}3}$). The sandy-loess and soil layers are supposed to deposit instantaneously. Model 2 gives a time of exposure of the conglomerate without shielding of 2.7 ka, thus an abandonment age of 14.9 ka ($t_{2\text{-}1}$). A third model (model 3), is similar to model 2 but instead of considering an instantaneous deposition of the sandy-loess and soil layers, it considers progressive deposition of the shielding layers, the 30 cm of loess between 12.2 ka and 7.6 ka, (6.5 cm/ka) and the 80 cm-thick soil development between 7.6 ka until today (10.5 cm/ka). Model 3 is a minimum shielding model or minimum age model and gives an abandonment age of 13.7 ka ($t_{3\text{-}1}$). The results of the two latter models are similar within error bars, and we thus suggest an abandonment age for T3 of 13.7±1.5 ka.

For terraces T2 and T1, we collected surface samples, mostly pieces of the top of large boulders from the surface of the terraces. 7 samples were collected on T2, all on the part of the terrace located downstream from the fault (Figure 4, Table 3). 6 samples were collected on T1, 3 north of the fault and 3 south of the fault (Figure 4, Table 3). The exposure ages of T1 and T2 were calculated using the CRONUS calculator (Balco et al., 2008) with the time-dependent Lal (1991) / Stone (2000) scaling scheme for spallation (Table 3). Ages of T1 range from 1 to 14 ka with an average of 9.0±1.4 ka. Ages of T2 range from 10 to 39 ka with an average of 16.6±3.0 ka. Both age distributions on T2 and T1 indicate a large scatter in the data, with overlapping values between terraces (Figure 9), that may be related to unevenly

382 distributed and large inheritance among the boulders and/or variable erosion affecting
383 the protruding large boulders at the surface of the terraces. Such ^{10}Be concentration
384 scatter is a common feature of boulders originating from small size high-mountain
385 glacier catchments where accumulation and transport vary with climate changes (e.g.
386 Putkonen & Swanson, 2003; Heimsath & McGlynn, 2008; Heyman et al., 2011).
387 Boulders may have sat at various depths in moraines upstream at high elevation
388 during a large part of the Pleistocene, before being transported episodically thanks to
389 increased moist periods and during brief flash floods. Unlike large catchments with
390 deep valley fill, most of the conglomeratic material composing the fan and terraces at
391 the outlet of the upper valley across the fault zone were probably never buried deep
392 enough to be shielded completely from cosmic rays. The deepest gravels in the T3
393 depth profile have concentrations representing about 20 to 30% of the surface samples,
394 which represent a significant amount of inherited ^{10}Be acquired upstream. This
395 amount of inheritance may be indicative of the intermittent stream dynamics and
396 evidence of sediment accumulation in the catchment. Inheritance may be distributed
397 differently in amalgamated gravels and large blocks, as their mode of transport and
398 residence time in the catchment differ greatly (e.g. Benedetti and Van der Woerd,
399 2014; Carretier et al., 2015). Alternatively, the youngest boulder ages may correspond
400 to samples with minimal inheritance and thus closest to the true surface age (e.g., Le
401 Dortz et al., 2011; Owen et al., 2011), yielding 11.8±1.1 ka for T2 and 1.2±0.1 ka for
402 T1 (Figure 9). Additional age constraints for T2 may be given by the age of the
403 overlying soil determined by radiocarbon dating (Liang et al., 2018). The concordant
404 ages of 8.0-8.7 ka obtained in two soil pits upstream and downstream in T2 indicate
405 that T2 must have been abandoned at that time. Thus, the abandonment age of T2
406 must have occurred sometime between 8.0 and 11.8 ± 1.1 ka.
407
408 **Slip rate**

409 The difference between far field and near field offsets of the T3/T2 and T2/T1
410 risers indicates incomplete riser refreshing during lower level occupation. Near field
411 displacements of d3u, d3l, d2u and d2l exist. Furthermore d3u and d3l are similar to
412 the displacement of riser T2/T1 (D2u, D2l), and d2u and d2l are similar with the
413 stream offset Ds (Table 4). Therefore, offsets of risers T3/T2 and T2/T1 started to
414 accumulate before the lower terraces were abandoned (Figure 11). In addition, the
415 riser T3/T2 may have been further modified by incision of channel T2' at its base and
416 within level T2. The timing of abandonment of T2' is loosely constrained as
417 occurring after abandonment of T2 (i.e., 8-12 ka) and before deposition of T1 (i.e., 1.2
418 ka).
419 Dividing the average cumulative displacement of the crest of the T3/T2 riser of
420 88±9 m by the abandonment age of T3 of 13.7 ± 1.5 ka yields a minimum left-lateral
421 slip rate of 6.4±1.2 mm/yr (5.2-7.9 mm/yr). The cumulative displacement of the base
422 of the T3/T2 riser of 72±3 m may correspond to the emplacement of T2 at 8.0-11.8 ±
423 1.1 ka and yields a maximum slip rate of 7.3±2.0 mm/yr (5.3-9.4 mm/yr). The T2/T1
424 riser offset of 35±2 m at crest or 27±2 m at base, similar to the T2' channel offset of
425 29±2 m, remains unconstrained in the absence of ages for T2'.
426 Fault scarp heights across T3 and T2 and corresponding ages may be used to
427 estimate the vertical slip rate. For T3, dividing the throw of profile C-C' of 15±2 m by
428 its abandonment age of 13.7±1.5 ka yields a vertical slip rate of 1.1±0.3 mm/yr. For
429 T2, dividing the throw of profile B-B' of 10±1 m by its abandonment age of 8.0-11.8
430 ±1.1 ka yields a similar vertical slip rates of 0.7-1.4 mm/yr. The average vertical slip
431 rate is 1.1±0.3 mm/yr (Figure 12).
432 Given the vertical offsets of T2' of 5-7 m, and assuming a constant vertical slip
433 rate of 1.1±0.3 mm/yr, the age of T2' may be estimated to be about 5.4±1 ka.
434 Similarly, the age of T1 offset 1.3±0.2 m may be estimated at about 1.2±0.2 ka,
435 concordant with the youngest surface exposure age.

Relating these less well constrained and indirectly determined ages for T2' and T1, with the corresponding offsets of T2' of 29±2 m and T1 of 6.5 m, yields rates of 5.3± 1.5 mm/yr and 5.4±1.3 mm/yr, respectively.

DISCUSSION

Variability in slip rate determination

Geologic fault slip rate reflects the long-term fault behavior, it is thus a basic datum for understanding strain accommodation through a system of faults, and also one of the most important indicators for earthquake potential of a fault. Considerable efforts have been devoted to determining the slip rate on active faults within the Tibetan Plateau. Geologic determination of fault slip rate is simple in principle but is subject to considerable uncertainty. The difficulty lies in the fact that the duration of offset accumulation is often approximated by a surrogate age. For instance, terrace risers are commonly used as offset features in slip rate determination of faults in northern Tibet, including the Haiyuan, the Altyn Tagh and the Kunlun faults (e.g. Cowgill et al., 2009; Kirby et al., 2007; Lasserre et al., 1999; Mériaux et al., 2004, 2005, 2012; Van der Woerd et al., 1998, 2000; Meyer et al., 1996; Peltzer et al., 1988). They are erosive features, which likely form diachronously, starting to record offset sometime after the abandonment of the upper terrace and before the abandonment of the lower terrace (e.g., Ryerson et al., 2006). The abandonment age of the upper terrace surface provides the maximum age of slip accumulation, thus the lower bound of the true slip rate. Accordingly, the lower terrace surface age represents the minimum age of slip accumulation and thus the upper bound of the slip rate.

The difference in geologic slip rate on the Haiyuan fault stems mainly from this uncertainty of using upper terrace surface versus lower terrace surface age as the surrogate for the true offset age of the terrace riser. Lasserre et al. (2002) reported 12 ± 4 mm/yr on the eastern Maomao Shan (Laohu Shan) sections of the Haiyuan fault. They used the lower terrace age, i.e., the minimum age for offset accumulation, thus

464 provided an upper bound for the slip rate. On the other hand, much lower slip rates
465 were reported, 3.3-6.6 mm/yr on the Lenglongling section (He et al., 2000, 2010;
466 Jiang et al., 2017), and 4.1-5.8 mm/yr on the Laohu Shan section (Yuan et al., 1998),
467 respectively. These lower rates are based on the scenario of using the upper terrace
468 surface age for slip accumulation, and thus provide the lower bound of the slip rate.
469 As shown in the summary of Table S1, studies along the Haiyuan fault showing slip
470 rate less than 5 mm/yr are mainly based on an upper terrace reconstruction. In a few
471 cases both the upper and lower terraces were dated (Li et al., 2009; Zheng et al.,
472 2013). If the lower terrace reconstruction scenario is considered, an upper bound in
473 the range of 4.5-22 mm/yr is implied, even though this upper bound is not mentioned
474 in these studies (Table S1). An objective evaluation of these two previous studies
475 show that these studies sampled the loess cover (either OSL or 14C dating) of the
476 upper terrace surface, which postdated the abandonment of the terrace surface. The
477 implication is that even though the upper terrace constrains the maximum age of
478 offset accumulation, the loess cover shifts the age to be younger. Eventually,
479 considering these factors, many slip rate determinations should have larger
480 uncertainty than reported. It is tempting to favor the lower bound estimates for the
481 Haiyuan fault, as it is closer to the geodetic rates from GPS velocity field of 4-5
482 mm/yr (Li et al, 2009) or from InSAR data of 4-8 mm/yr (Cavalié et al., 2008; Jolivet
483 et al., 2012; Daout et al., 2016), as in the case of the Altyn Tagh fault (Cowgill, 2007;
484 Zhang et al., 2007; Gold et al., 2009, 2011a). However, high GPS loading rate of 8.6
485 mm/yr was also reported on the Haiyuan fault (Gan et al., 2007), as well as high rate
486 from InSAR of 8.6±1.5 mm/yr along the central section (Daout et al., 2016). These
487 data remind us that the current GPS field is not targeted for optimal determination of
488 fault loading rate, because GPS sites are still sparse, and thus the strain rate across the
489 fault must be estimated by collapsing all measurements within a wide (often 100 km
490 wide) swath. When doing so, the effects of fault geometry changes along strike are

not taken into account, which could be important for explaining the considerable lateral and gradual variation in the regional GPS velocity field.

Strictly speaking, the true slip rate of the Haiyuan fault should lie between the ranges of upper and lower bounds. It is helpful to resolve the variability to explicitly distinguish the lower and upper bounds when reporting the rate. At the Daqing site in this study, the upper and the lower bounds of the slip rate constrained by T3/T2 terrace riser are remarkably similar, 6.4 mm/yr and 7.3 mm/yr. This is because the ages of T3 (13.7 ka) and T2 (8.0-11.8 ka) might be relatively close in time.

T2/T1 terrace riser, on the other hand, provides a much larger uncertainty and looser constraint on the slip rate (3.3-23.5 mm/yr) when neglecting T2' (Figure 12B). The contrast in slip rate bracketed by T3/T2 and T2/T1 at the same site highlights again that one should not favor the upper or the lower terrace reconstruction scenarios, without additional information. If we use the upper terrace age as the offset age, the offset of T3/T2 riser suggests a slip rate of 6.4 mm/yr (since 13.7 ka), whereas the offset of T2/T1 riser suggests 3.3 mm/yr (since 8.0-11.8 ka), almost two times lower. This difference at the same site could be interpreted as a temporal change in slip rate, as suggested elsewhere in some previous studies (Gold et al., 2017; Liu et al., 2018). In reality, the rates given are simply the lower bound, rather than the true slip rate. The difference is a good indication of variable initiation time of riser offset record after the abandonment of the upper terrace, thus the uncertainty in slip rate determination, rather than an indication of temporal change in slip behavior. In fact, the comparison between short term and long term slip rate for a number of large strike-slip faults all over the world also shows that the slip rate is not changing significantly through time (Cowgill et al., 2009; Meade et al., 2013; Tong et al, 2014).

The assumption of uniform slip rate over time implies that the slip vector should be temporally stable. Thus, the ratio of vertical and horizontal offsets is also consistent on each terrace. The vertical offset of 15±2 m and the minimum horizontal offset of 88±9 m on T3 imply a maximum ratio of 0.17±0.04. The ratios are

519 0.21±0.05 and 0.2±0.05 on T2' and T1, respectively. We constrain an average ratio of
520 0.16±0.01 consistent with the range of ratios for the three terraces.

521 The ratio of 0.125±0.025 estimated by Gaudemer et al. (1995) is a little smaller
522 than the average ratio of 0.16±0.01 (Figure 13). This is due to a larger total horizontal
523 displacement of the upper terrace (T3, 145 m) estimated from the assumption of lower
524 terrace reconstruction. As we discuss above, the horizontal offset of the upper riser
525 can only define an upper bound of the displacement of the lower terrace, suggesting
526 that the ratio of 0.125±0.025 is in the low range.

527 Furthermore, when combining the ratio of 0.16±0.01 and the vertical offset of
528 10±1m on T2, we can estimate the total displacement of T2 to about 63±10m, which
529 is much larger than the riser T2/T1 offset (35±2 m) and similar to the minimum offset
530 of T3/T2 (72±2 m).

531 Following the assumption of a temporally stable deformation rate, we summarize
532 the measured offsets versus corresponding ages (Figure 14), and propose a broadly
533 uniform strike slip rate of 5-8 mm/yr. The tightly constrained age of T3 and the far
534 field offset of the lower riser (solid rectangle) have much more weight in the
535 determination of the rate than other less well determined data (dashed rectangles).

536 Our investigation at the Daqing site shows that incomplete riser refreshment and
537 slip accumulation before the lower terrace abandonment can also occur on the
538 unprotected side of the river bank. A terrace riser on the left bank of a river across a
539 left-lateral fault would be on the protected side, i.e., continuous left-lateral slip would
540 move the downstream section of the riser away from the stream center and be less
541 frequently refreshed, thus more likely to record offset before the abandonment of the
542 lower terrace abandonment (e.g., Cowgill, 2007). At the same time, if a terrace riser
543 on the right bank was developed, left-lateral slip on the fault would move the
544 downstream part of the riser toward the center and in alignment with the upstream
545 channel. This configuration would favor more frequent riser refreshment and
546 obliteration of offset before the abandonment of the lower terrace (e.g., Van der

547 Woerd et al., 1998; Tapponnier et al., 2001). However, our offset measurements and
548 dating of sequentially abandoned terrace surfaces suggests that right-bank terrace riser
549 on a left-lateral fault, i.e., erosive side, is also subject to incomplete riser refreshment
550 and partial preservation of offset before the abandonment of the lower terrace. The
551 lower terrace reconstruction may not be a safe assumption even for this favorable
552 riser-offset configuration. The obliquity in slip vector and the accumulation of vertical
553 displacement inducing strong incision in the upstream terrace deposits (Figure 8) may
554 increase channeling upstream and less erosion downstream. The terrace riser
555 development and preservation remain complex processes, including diachroneity and
556 different age of riser sections on opposite sides of the fault related to fluvial erosion
557 and riser degradation (e.g., Harkins and Kirby, 2008; Gold et al., 2009, 2011b).
558
559 **Earthquake rupture implication**
560 The youngest exposure age on terrace T1 is 1.1 ± 0.1 ka, which implies that the
561 age of the most recent rupture at this site should be younger than 1.1 ± 0.1 ka, but
562 may be older than eight centuries (Gaudemer et al., 1995). Trenching by Yuan et al.
563 (1997) indicated three events on the Jinqiang He section near our site with the most
564 recent event around 1000 a B.P. This result may give some clue about the latest
565 rupture, even though details about the trench interpretations are lacking. The two
566 older events presented might rupture both the Jianqiang He and western part of the
567 Maomao Shan sections around ~1800 ka B.P. and ~4000 yr B.P. The Lenglongling
568 section, west of our site, has a mean event recurrence interval of 1430 ± 140 a during
569 the Holocene (Jiang et al., 2017) or 1640 ± 570 a (Guo et al., 2019). To the east of our
570 site, the Laohu Shan section seemingly ruptures every ~1000 a (Yuan et al., 1997;
571 Liu-Zeng et al., 2007). If T1 and T0 experienced only one rupturing event with the
572 scarp on T0 being almost completely eroded, the offset of ~6.0 ± 0.5 m of the
573 abandoned stream channel present on T1 may preserve the last coseismic lateral slip.
574 Using the slip rate of 5-8 mm/yr and this coseismic offset, the average recurrence

575 interval would be 1100±300 a, consistent with other studies. We speculate the
576 Jinqiang He section has similar rupture history with recurrence interval of 1000-1500
577 a and the most recent rupture about 1000 a.

578 The Jinqiang He section, called Tianzhu seismic gap by Gaudemer et al. (1995),
579 is about 55 km long. If this section ruptured entirely, the magnitude could reach Mw
580 7.4 to 7.7 according to empirical relationship between magnitude, surface rupture
581 length and average displacement, respectively, for strike slip faults (Wells and
582 Coppersmith, 1994). It is likely that a rupture on the Jinqiang He section could breach
583 the Tianzhu stepover and propagate to the western part of the Maomao Shan section.
584 The rupture length would reach ~120 km, and the maximum magnitude would be Mw
585 7.8 (Wells and Coppersmith, 1994). The Jinqiang He and adjacent sections could be
586 ripe for rupturing in a future great earthquake. Precise seismic risk assessment
587 demands that further detailed paleoseismical investigations be carried out to define a
588 more accurate rupture history along the central Haiyuan fault.
589

590 ## CONCLUSION

591 High resolution topography data derived from the terrestrial LiDAR enable us to
592 investigate offset features of the Haiyuan fault in detail. Based on T1, T2 and T3
593 terraces mapped carefully from topography data, we use local fitting piercing lines to
594 estimate the range of displacement for T3/T2 to be 88±9 m at the crest and 72±3 m at
595 the base, and for T2/T1 to be 27±2 - 35±2 m. Maximum vertical throw for T3, T2 and
596 T2' is 15±2 m, 10± 1 m and 6±1 m respectively. The vertical motion on T1 was also
597 estimated to be 1.3±0.2 m. The total strike displacement of T3 is larger than 88±9 m,
598 T2 is between 72±3 m and 35±2 m, or 63±10 m derived from relationship of vertical
599 and horizontal offset. The channel T2' incised in T2 is horizontally offset 29±2 m.
600 The horizontally offset small stream on T1 and near field offset of riser T2/T1
601 indicate the total strike displacement of T1 is 6.5±1 m. The offset of 6.0 ± 0.5 m of
602 the small stream may be associated with the most recent slip event. Terrestrial

603 Cosmogenic nuclides dating, combined with ^{14}C and OSL dating, were used to
604 constrain the age of T3 at 13.7±1.5 ka. These data suggest a slip rate of 6.6±1.4
605 mm/yr since 15 ka. T2 and T1, are less well constrained at 8.0-11.8±1.1 ka and 1.1±
606 =0.1 ka, respectively. Assuming a constant vertical to horizontal ratio, the age of T2'
607 may be inferred at 5.4±1 ka. The slip rate of 5-8 mm/yr is broadly consistent with all
608 data. This slip rate is similar to the recent reassessment of the slip rate (5.0-8.9 mm/yr)
609 near Songshan (Yao et al., 2019).
610

611 ## ACKNOWLEDGMENTS

612 This work is jointly funded by the Science for Earthquake Resilience of China
613 Earthquake Administration (XH19044), the National Natural Science Foundation of
614 China (41802228, ###). YS has been partly supported by a grant from K.C. Wong
615 Fundation and CNRS. YK is partly supported by China – France PICS program from
616 CNRS. GF-1 satellite imagery was offered by Dr. Wang Lin from Institute of
617 Earthquake Science, China Earthquake Administration. We thank Alex Morelan and
618 Veronica Prush in UC Davis for their advice on sample ages analysis. We are grateful
619 to ASTER Team (G. Aumai□tre, D. Bourlès, and K. Keddadouche) at
620 ASTER-CEREGE for AMS measurements. This work was financially supported by
621 the INSU-CNRS, France and the University of Strasbourg to J. Van der Woerd for the
622 Al and Be concentration analyses at LHyGeS and IPGS, and for 10Be/9Be and
623 26Al/27Al ratios measurements on the Aster AMS facility (GEREGE,
624 Aix-en-Provence, France) supported by INSU-CNRS and IRD.

625

626 **REFERENCES CITED**

627 Arrowsmith, J R., and O. Zielke, 2009. Tectonic geomorphology of the San Andreas
628 fault zone from High Resolution Topography: an example from the Cholame
629 Section. Geomorphology. 113, 70-81, doi:10.1016/j.geomorph.2009.01.002.

630 Balco, G., Stone, J. O., Lifton, N. A., & Dunai, T. J., 2008. A complete and easily
631 accessible means of calculating surface exposure ages or erosion rates from 10 Be
632 and 26Al measurements. Quaternary geochronology. 3(3), 174-195.
633 Bendick, R., Bilham, R., Freymueller, J., Larson, K., and Yin, G., 2000, Geodetic
634 evidence for a low slip rate in the Altyn Tagh fault system: Nature, v. 404, p. 69–
635 72, doi: 10.1038/35003555.
636 Berryman, K., 1990. Late Quaternary movement on the Wellington fault in the Upper
637 Hutt area, New Zealand. New Zealand journal of geology and geophysics, 33(2),
638 pp.257-270.
639 Burchfiel, B.C., Quidong, D., Molnar, P., Royden, L., Yipeng, W., Peizhen, Z. and
640 Weiqi, Z., 1989. Intracrustal detachment within zones of continental deformation.
641 Geology, 17(8), pp.748-752.
642 Burchfiel, B.C., Peizhen, Z., Yipeng, W., Weiqi, Z., Fangmin, S., Qidong, D., Molnar,
643 P. and Royden, L., 1991. Geology of the Haiyuan fault zone, Ningxia-Hui
644 autonomous region, China, and its relation to the evolution of the northeastern
645 margin of the Tibetan plateau. Tectonics. 10, doi: 10.1029/90TC02685.
646 Cavalié, O., Lasserre,C., Doin, M.-P., Peltzer, G., Sun, J., Xu, X., Shen, Z.-K., 2008.
647 Measurement of interseismic strain across the Haiyuan fault (Gansu, China), by
648 InSAR. Earth Planet. Sci. Lett. doi:10.1016/j.epsl.07.057.
649 Chen, T., Zhang, P. Z., Liu J., Li, C. Y., Ren, Z. K., Hudnut, K. W., 2014.
650 Quantitative study of tectonic geomorphology along Haiyuan fault based on
651 airborne LiDAR. Chinese Science Bulletin. 59(20): 2396-2409,
652 doi:10.1007/s11434-014-0199-4.
653 Chen, T., Akciz, S.O., Hudnut, K.W., Zhang, D.Z. and Stock, J.M., 2015. Fault-Slip
654 Distribution of the 1999 Mw 7.1 Hector Mine Earthquake, California, Estimated
655 from Postearthquake Airborne LiDAR Data. Bull. Seismol. Soc. Am. 105(2A),
656 776-790.

657 Chevalier, M.L., Leloup, P.H., Replumaz, A., Pan, J., Liu, D., Li, H., Gourbet, L. and
658 Métois, M., 2016. Tectonic-geomorphology of the Litang fault system, SE Tibetan
659 Plateau, and implication for regional seismic hazard. Tectonophysics, 682,
660 pp.278-292.
661 Clark, K., E. Nissen, J. Howarth, I. Hamling, J. Mountjoy, W. Ries, K. Jones, S.
662 Goldstein, U. Cochran, P. Villamor, S. Hreinsdóttir, N. Litchfield, C. Mueller, K.
663 Berryman, D. Strong. 2017. Highly variable coastal deformation in the 2016 Mw
664 7.8 Kaikōura earthquake reflects rupture complexity along a transpressional plate
665 boundary, Earth Planet. Sci. Lett. 474, 334–344.
666 Cowgill, E., 2007, Impact of riser reconstructions on estimation of secular variation in
667 rates of strike-slip faulting: revisiting the Cherchen River site along the Altyn Tagh
668 Fault, NW China: Earth and Planetary Science Letters, v. 254, p. 239–255, doi:
669 10.1016/j.epsl.2006.09.015.
670 Cowgill, E., Gold, R.D., Xuanhua, C., Xiao-Feng, W., Arrowsmith, J.R. and Southon,
671 J., 2009. Low Quaternary slip rate reconciles geodetic and geologic rates along the
672 Altyn Tagh fault, northwestern Tibet. Geology, 37(7), pp.647-650.
673 Daout, S., Jolivet, R., Lasserre, C., Doin, M.P., Barbot, S., Tapponnier, P., Peltzer, G.,
674 Socquet, A. and Sun, J., 2016. Along-strike variations of the partitioning of
675 convergence across the Haiyuan fault system detected by InSAR. Geophysical
676 Journal International, 205, 536–547. https://doi.org/10.1093/gji/ ggw028
677 Deng, Q., Sung, F., Zhu, S., Li, M., Wang, T., Zhang, W., Burchfiel, B.C., Molnar, P.
678 and Zhang, P., 1984. Active faulting and tectonics of the Ningxia-Hui autonomous
679 region, China. Journal of Geophysical Research, 89, 4427-4445.
680 Duvall, A.R., Clark, M.K., Kirby, E., Farley, K.A., Craddock, W.H., Li, C. and Yuan,
681 D.Y., 2013. Low-temperature thermochronometry along the Kunlun and Haiyuan
682 Faults, NE Tibetan Plateau: Evidence for kinematic change during late-stage
683 orogenesis. Tectonics, 32(5), pp.1190-1211.

684 Elliott, J.R., Biggs, J., Parsons, B., and Wright, T.J., 2008, InSAR slip rate deter-
685 minations on the Altyn Tagh Fault, northern Tibet, in the presence of topo-
686 graphically correlated atmospheric delays: Geophysical Research Letters, v. 35,
687 L12309, doi: 10.1029/2008GL033659.
688 England, P. and Molnar, P., 1997. The field of crustal velocity in Asia calculated from
689 Quaternary rates of slip on faults. Geophys. J. Int. 130(3), 551-582.
690 Galbraith, R.F. and Roberts, R.G., 2012. Statistical aspects of equivalent dose and
691 error calculation and display in OSL dating: an overview and some
692 recommendations. Quaternary Geochronology. 11, 1-27.
693 Gan, W., Zhang, P.Z., Shen, Z.-K., Niu, Z., Wang, M., Wan, Y., Zhou, D., Cheng, J.,
694 2007. Present-day crustal motion within the Tibetan Plateau inferred from GPS
695 measurements. J. Geophys. Res. 112 (B8). doi:10.1029/2005JB004120.
696 Gaudemer, Y., Tapponnier, P., Meyer, B., Peltzer, G., Guo Shunmin, Chen Zhitai,
697 Dai Huagung and Cifuentes, I., 1995. Partitioning of crustal slip between
698 linked, active faults in the eastern Qilianshan, and evidence for a major seismic
699 gap, the 'Tianzhu gap',on the western Haiyuan fault, Gansu(China). Geophys. J.
700 Int. 120:599-645.
701 Gold, R.D., Cowgill, E., Arrowsmith, J.R., Gosse, J., Chen, X., and Wang, X.- F.,
702 2009, Riser diachroneity, lateral erosion, and uncertainty in rates of strike-slip
703 faulting: A case study from Tuzidun along the Altyn Tagh Fault, NW China:
704 Journal of Geophysical Research: Solid Earth, 114(B4). doi:
705 10.1029/2008JB005913
706 Gold, R.D., Cowgill, E., Arrowsmith, J.R., Chen, X., Sharp, W.D., Cooper, K.M. and
707 Wang, X.F., 2011a. Faulted terrace risers place new constraints on the late
708 Quaternary slip rate for the central Altyn Tagh fault, northwest Tibet. Bulletin,
709 123(5-6), 958-978.

710 Gold, R.D. and Cowgill, E., 2011b. Deriving fault-slip histories to test for secular
711 variation in slip, with examples from the Kunlun and Awatere faults. Earth and
712 Planetary Science Letters, 301(1-2), pp.52-64.
713 Gold, R.D., Cowgill, E., Arrowsmith, J.R. and Friedrich, A.M., 2017. Pulsed strain
714 release on the Altyn Tagh fault, northwest China. Earth and Planetary Science
715 Letters, 459, 291-300.
716 Guo, P., Han, Z., Mao, Z., Xie, Z., Dong, S., Gao, F. and Gai, H., 2019.
717 Paleoearthquakes and rupture behavior of the Lenglongling fault: Implications for
718 seismic hazards of the northeastern margin of the Tibetan Plateau. Journal of
719 Geophysical Research: Solid Earth. https://doi.org/10.1029/2018JB016586
720 Harkins, N., and Kirby, E., 2008, Fluvial terrace riser degradation and determination
721 of slip rates on strike-slip faults: An example from the Kunlun fault, China: Geo-
722 physical Research Letters, v. 35, no. L05406, 6 p., doi: 10.1029/2007GL033073.
723 He Wengui, Liu Baichi, Yuan Daoyang, and Yang Ming, 2000. Study on the slip rate
724 of Lenglongling active fault zone, Northwestern Seismological Journal.
725 22(1):90-97 (in Chinese).
726 He, W.G., Yuan, D.Y., Ge, W.P. and Luo, H., 2010. Determination of the slip rate of
727 the Lenglongling Fault in the middle and eastern segments of the Qilian Mountain
728 active fault zone. Earthquake, 30(1), pp.131-137 (in Chinese).
729 Heimsath, A.M. and McGlynn, R., 2008. Quantifying periglacial erosion in the Nepal
730 high Himalaya. Geomorphology, 97(1-2), pp.5-23.
731 Heyman, J., Stroeven, A.P., Harbor, J.M., Caffee, M.W., 2011. Too young or too old:
732 evaluating cosmogenic exposure dating based on an analysis of compiled boulder
733 exposure ages. Earth and Planetary Science Letters 302, 71–80.
734 Hetzel, R., 2013. Active faulting, mountain growth, and erosion at the margins of the
735 Tibetan Plateau constrained by in situ-produced cosmogenic nuclides.
736 Tectonophysics, 582, pp.1-24.

737 Hudnut, K.W., Borsa, A., Glennie, C. and Minster, J.B., 2002. High-resolution
738 topography along surface rupture of the 16 October 1999 Hector Mine, California,
739 earthquake (Mw 7.1) from airborne laser swath mapping. Bull. Seismol. Soc. Am.
740 92(4), 1570-1576.
741 Jiang, W., Han, Z., Guo, P., Zhang, J., Jiao, Q., Kang, S. and Tian, Y., 2017. Slip rate
742 and recurrence intervals of the east Lenglongling fault constrained by
743 morphotectonics: Tectonic implications for the northeastern Tibetan Plateau.
744 Lithosphere, 9(3), pp.417-430.
745 Kirby, E., Harkins, N., Wang, E., Shi, X., Fan, C., and Burbank, D. (2007), Slip rate
746 gradients along the eastern Kunlun fault, Tectonics, 26, TC2010,
747 doi:10.1029/2006TC002033.
748 Klinger, Y., Etchebes, M., Tapponnier, P. and Narteau, C., 2011. Characteristic slip
749 for five great earthquakes along the Fuyun fault in China. Nature Geoscience. 4(6),
750 389-392.
751 Knuepfer, P.L., 1992. Temporal variations in latest Quaternary slip across the
752 Australian-Pacific plate boundary, northeastern South Island, New Zealand.
753 Tectonics, 11(3), pp.449-464.
754 Küster, Y., Hetzel, R., Krbetschek, M. and Tao, M., 2006. Holocene loess
755 sedimentation along the Qilian Shan (China): significance for understanding the
756 processes and timing of loess deposition. Quat. Sci. Rev. 25(1), 114-125.
757 Lal, D., 1991. Cosmic ray labeling of erosion surfaces: in situ nuclide production rates
758 and erosion models. Earth and Planetary Science Letters 104, 424e439.
759 Langridge, R. M., Rowland, J., Villamor, P., Mountjoy, J., Townsend, D. B., Nissen,
760 E., Madugo, C., Ries, W. F., Gasston, C., Canva, A., Alexandra E. Hatem, A. E.,
761 Hamling, I. 2018. Coseismic rupture and preliminary slip estimates for the Papatea
762 Fault and its role in the 2016 Mw 7.8 Kaikōura, New Zealand, Earthquake.
763 Bulletin of the Seismological Society of America, 108(3B), 1596-1622.

764 Lasserre C. , Morel P.H. , Gaudemer Y. , Tapponnier P., Ryerson F.J., King G.C.P.,
765 Mtivier F., Kasser M., Kashgariana M., Liu Baichi, Lu Taiyi, Yuan Daoyang, 1999.
766 Postglacial left slip rate and past occurrence of M≥8 earthquakes on the western
767 Haiyuan fault, Gansu, China. J. Geophys. Res. 104, B8, 17633-17651.
768 Lasserre C., Gaudemer Y., Tapponnier P., Me´riaux A.-S., Woerd J.Van der, Yuan
769 Daoyang, Ryerson F. J., Finkel R. C., and Caffee M.W., 2002. Fast late Pleistocene
770 slip rate on the Lenglongling section of the Haiyuan fault, Qinghai, China. J.
771 Geophys. Res. 107(B11):2276.
772 Le Béon, M., Klinger, Y., Mériaux, A.S., Al-Qaryouti, M., Finkel, R.C., Mayyas, O.
773 and Tapponnier, P., 2012. Quaternary morphotectonic mapping of the Wadi Araba
774 and implications for the tectonic activity of the southern Dead Sea fault. Tectonics,
775 31(5). doi:10.1029/2012TC003112.
776 Le Dortz, K., Meyer, B., Sébrier, M., Braucher, R., Nazari, H., Benedetti, L., Fattahi,
777 M., Bourlès, D., Foroutan, M., Siame, L. and Rashidi, A., 2011. Dating inset
778 terraces and offset fans along the Dehshir Fault (Iran) combining cosmogenic and
779 OSL methods. Geophysical Journal International, 185(3), pp.1147-1174.
780 Lensen, G.J., 1968. Analysis of progressive fault displacement during downcutting at
781 the Branch River terraces, South Island, New Zealand. Geological Society of
782 America Bulletin, 79(5), pp.545-556.
783 Li, C., Zhang, P.Z., Yin, J. and Min, W., 2009. Late Quaternary left-lateral slip rate of
784 the Haiyuan fault, northeastern margin of the Tibetan Plateau. Tectonics. 28(5).
785 doi:10.1029/2008TC002302.
786 Liang Shumin, Zheng Wenjun, Chen Gan. 2018. Offset distribution and slip rate of
787 the Jinqianghe fault of the Qilian–Haiyuan fault zone. Annual meeting of Chinese
788 Geoscience Union, Abastract in Chinese.
789 Liu Jinrui, Ren Zhikun, Zhang Huiping, Li Chuanyou, Zhang Zhuqi, Zheng Wenjun,
790 Li Xuemei, Liu Caicai. 2018. Late Quaternary slip rate of the Laohushan fault

791 within the Haiyuan fault zone and its tectonic implications. Chinese Journal Of
792 Geophysics,61(4): 1281-1297, doi: 10.6038/cjg2018L0364 (in Chinese).
793 Liu-Zeng, J., Klinger, Y., Xu, X., Lasserre, C., Chen, G., Chen, W., Tapponnier, P.
794 and Zhang, B., 2007. Millennial recurrence of large earthquakes on the Haiyuan
795 fault near Songshan, Gansu Province, China. Bulletin of the Seismological Society
796 of America, 97(1B), 14-34.
797 Liu-Zeng,J., Chen T,Zhang P. Z., Zhang H. P., Zheng W. J., Ren Z K, Liang S. M.,
798 Shen C. S., Gan W.J. 2013. Illuminating the active Haiyuan fault, China by
799 AirborneLight Detection and Ranging. Chinese Science Bulletin. 58: 41-45, doi:
800 10.1360/972012-1526 (in Chinese).
801 Liu-Zeng, J., Shao, Y., Klinger, Y., Xie, K., Yuan, D. and Lei, Z., 2015. Variability in
802 magnitude of paleoearthquakes revealed by trenching and historical records, along
803 the Haiyuan Fault, China. Journal of Geophysical Research: Solid Earth, 120(12),
804 8304-8333.
805 Loveless, J., Meade, B., 2011. Partitioning of localized and diffuse deformation in the
806 Tibetan plateau from joint inversions of geologic and geodetic observations. Earth
807 Planet. Sci. Lett. 303 (1–2), 11–24.
808 Matrau, R., Y. Klinger1, J. Van der Woerd, J. Liu-Zeng, Z. Li, X. Xu, and R. Zheng.
809 2019. Late Pleistocene-Holocene slip rate along the Hasi Shan restraining bend of
810 the Haiyuan fault: implication for faulting dynamics of a complex fault system,
811 Tectonics, doi: 10.1029/2019TC005488.
812 McGill, S.F., Owen, L.A., Weldon, R.J. and Kendrick, K.J., 2013. Latest Pleistocene
813 and Holocene slip rate for the San Bernardino strand of the San Andreas fault,
814 Plunge Creek, Southern California: Implications for strain partitioning within the
815 southern San Andreas fault system for the last~ 35 ky. Bulletin, 125(1-2),
816 pp.48-72.
817 Meade, B.J., Klinger, Y. and Hetland, E.A., 2013. Inference of multiple earthquake-
818 cycle relaxation timescales from irregular geodetic sampling of interseismic

819 deformation. Bulletin of the Seismological Society of America, 103(5),
820 pp.2824-2835.
821 Mériaux, A.-S., Ryerson, F.J., Tapponnier, P., Van der Woerd, J., Finkel, R.C., Xu, X.,
822 Xu, Z., and Caffee, M.W., 2004, Rapid slip along the central Altyn Tagh fault:
823 Morphochronologic evidence from Cherchen He and Sulamu Tagh: Journal of
824 Geophysical Research, v. 109, B06401, doi: 10/1029/2003jb002558.
825 Mériaux, A.S., Tapponnier, P., Ryerson, F.J., Xu, X.W., King, G., Van der Woerd, J.,
826 Finkel, R.C., Li, H.B., Caffee, M.W., Xu, Z.Q., Chen, W.B., 2005. The Aksay
827 section of the northern Altyn Tagh fault: tectonic geomorphology, landscape
828 evolution, and Holocene slip rate. J. Geophys. Res. -Solid Earth 110 (B4), B04404.
829 Métivier, F., Gaudemer, Y., Tapponnier, P. and Meyer, B., 1998. Northeastward
830 growth of the Tibet plateau deduced from balanced reconstruction of two
831 depositional areas: The Qaidam and Hexi Corridor basins, China. Tectonics, 17(6),
832 pp.823-842.
833 Meyer, B., Tapponnier, P., Gaudemer, Y., Peltzer, G., Guo, S., Chen, Z., 1996. Rate
834 of left-lateral movement along the easternmost segment of the Altyn Tagh Fault,
835 east of 96ºE (China). Geophys. J. Int. 124, 29-44.
836 Meyer, B., Tapponnier, P., Bourjot, L., Metivier, F., Gaudemer, Y., Peltzer, G.,
837 Shunmin, G. and Zhitai, C., 1998. Crustal thickening in Gansu-Qinghai,
838 lithospheric mantle subduction, and oblique, strike-slip controlled growth of the
839 Tibet plateau. Geophysical Journal International, 135(1), pp.1-47.
840 Middleton, T.A., Walker, R.T., Parsons, B., Lei, Q., Zhou, Y. and Ren, Z., 2016. A
841 major, intraplate, normal - faulting earthquake: The 1739 Yinchuan event in
842 northern China. J. Geophys. Res. Solid Earth. 121(1), 293-320.
843 Min, W., P. Zhang, Q. Deng, and F. Mao. 2001. Detailed study of Holocene
844 paleoearthquakes of the Haiyuan active fault, Geol. Rev., 47(1), 75–81.

845 Oskin, M. E., K. Le, and M. D. Strane, 2007. Quantifying fault-zone activity in arid
846 environments with high-resolution topography. Geophys. Res. Lett. 34, L23S05,
847 doi:10.1029/2007GL031295.
848 Oskin, M.E., Arrowsmith, J.R., Corona, A.H., Elliott, A.J., Fletcher, J.M., Fielding,
849 E.J., Gold, P.O., Garcia, J.J.G., Hudnut, K.W., Liu-Zeng, J. and Teran, O.J., 2012.
850 Near-field deformation from the El Mayor–Cucapah earthquake revealed by
851 differential LiDAR. Science. 335(6069), 702-705.
852 Owen, L.A., Frankel, K.L., Knott, J.R., Reynhout, S., Finkel, R.C., Dolan, J.F. and
853 Lee, J., 2011. Beryllium-10 terrestrial cosmogenic nuclide surface exposure dating
854 of Quaternary landforms in Death Valley. Geomorphology, 125(4), pp.541-557.
855 Peltzer, G., Tapponnier, P. and Armijo, R., 1989. Magnitude of late Quaternary
856 left-lateral displacements along the north edge of Tibet. Science, 246(4935),
857 pp.1285-1289.
858 Perrineau, A., Van Der Woerd, J., Gaudemer, Y., Liu-Zeng, J., Pik, R., Tapponnier, P.,
859 Thuizat, R. and Rongzhang, Z., 2011. Incision rate of the Yellow River in
860 Northeastern Tibet constrained by 10Be and 26Al cosmogenic isotope dating of
861 fluvial terraces: implications for catchment evolution and plateau building.
862 Geological Society, London, Special Publications, 353(1), 189-219.
863 Putkonen, J. and Swanson, T., 2003. Accuracy of cosmogenic ages for moraines.
864 Quaternary Research, 59(2), 255-261.
865 Ran, Y., R. Duan, and Q. Deng. 1997. 3-D trench excavation and paleoseismology at
866 Gaowanzi of the Haiyuan Fault, Earthquake Geol., 19(2), 97-107(in Chinese with
867 English abstract).
868 Rodgers, D.W. and Little, T.A., 2006. World's largest coseismic strike-slip offset: The
869 1855 rupture of the Wairarapa Fault, New Zealand, and implications for
870 displacement/length scaling of continental earthquakes. Journal of Geophysical
871 Research: Solid Earth, 111(B12).

872 Ryerson, F.J., Tapponnier, P., Finkel, R.C., Meriaux, A., Van der Woerd, J., Lasserre,
873 C., Chevalier, M., Xu, X.W., Li, H.B. and King, G.C., 2006. Applications of
874 morphochronology to the active tectomics of Tibet. SPECIAL
875 PAPERS-GEOLOGICAL SOCIETY OF AMERICA, 415, p.61.
876 Shen, Z.-K., Wang, M., Li, Y., Jackson, D.D., Yin, A., Dong, D., and Fang, P., 2001,
877 Crustal deformation along the Altyn Tagh fault system, western China, from GPS:
878 Journal of Geophysical Research, v. 106, p. 30,607-30,621, doi:
879 10.1029/2001JB000349.
880 Sieh, K.E., 1981. A review of geological evidence for recurrence times of large
881 earthquakes (No. 4, pp. 181-207). Washington, DC: American Geophysical Union.
882 Stokes, S., Hetzel, R., Bailey, R.M. and Mingxin, T., 2003. Combined IRSL-OSL
883 single aliquot regeneration (SAR) equivalent dose (De) estimates from source
884 proximal Chinese loess. Quaternary Science Reviews, 22(10), pp.975-983.
885 Stone, J.O., 2000. Air pressure and cosmogenic isotope production. Journal of
886 Geophysical Research 105, 23753e23759.
887 Stuiver M. and P.J. Reimer, 1993. Extended 14C data base and revised CALIB 3.0
888 14C Age calibration program. Radiocarbon. 35(1) 215-230.
889 Tapponnier, P. and Molnar, P., 1977. Active faulting and tectonics in China. J.
890 Geophys. Res. 82(20), 2905-2930.
891 Tapponnier, P., Meyer, B., Avouac, J.P., Peltzer, G., Gaudemer, Y., Shunmin, G.,
892 Hongfa, X., Kelun, Y., Zhitai, C., Shuahua, C. and Huagang, D., 1990. Active
893 thrusting and folding in the Qilian Shan, and decoupling between upper crust and
894 mantle in northeastern Tibet. Earth and Planetary Science Letters, 97(3-4),
895 pp.382-403.
896 Tapponnier, P., Zhiqin, X., Roger, F., Meyer, B., Arnaud, N., Wittlinger, G. and
897 Jingsui, Y., 2001a. Oblique stepwise rise and growth of the Tibet Plateau. Science,
898 294(5547), 1671-1677.

899 Tapponnier, P., Ryerson, F.J., Van Der Woerd, J., Mériaux, A.S. and Lasserre, C.,
900 2001b. Long-term slip rates and characteristic slip: keys to active fault behaviour
901 and earthquake hazard. Comptes Rendus de l'Académie des Sciences-Series
902 IIA-Earth and Planetary Science, 333(9).483-494.
903 Thackray, G.D., Rodgers, D.W. and Streutker, D., 2013. Holocene scarp on the
904 Sawtooth fault, central Idaho, USA, documented through lidar topographic
905 analysis. Geology. 41(6), 639-642.
906 Tong, X., Smith-Konter, B. and Sandwell, D.T., 2014. Is there a discrepancy between
907 geological and geodetic slip rates along the San Andreas Fault System?. Journal of
908 Geophysical Research: Solid Earth, 119(3), pp.2518-2538.
909 Van der Woerd J., F.J. Ryerson, P. Tapponnier, Y. Gaudemer, R. Finkel, A. S.
910 Mériaux, M. Caffee, Zhao Guoguang, He Qunlu, 1998. Holocene left-slip rate
911 determined by cosmogenic surface dating on the Xidatan section of the Kunlun
912 Fault (Qinghai, China), Geology, 26, 695-698.
913 Van Der Woerd, J., Ryerson, F.J., Tapponnier, P., Meriaux, A.S., Gaudemer, Y.,
914 Meyer, B., Finkel, R.C., Caffee, M.W., Guoguang, Z. and Zhiqin, X., 2000.
915 Uniform slip-rate along the Kunlun fault: Implications for seismic behaviour and
916 large-scale tectonics. Geophysical Research Letters, 27(16), pp.2353-2356.
917 Van der Woerd, J., Xu, X., Li, H., Tapponnier, P., Meyer, B., Ryerson, F.J., Meriaux,
918 A.S. and Xu, Z., 2001. Rapid active thrusting along the northwestern range front of
919 the Tanghe Nan Shan (western Gansu, China). Journal of Geophysical Research:
920 Solid Earth, 106(B12), pp.30475-30504.
921 Van der Woerd, J., Tapponnier, P., J. Ryerson, F., Meriaux, A.S., Meyer, B.,
922 Gaudemer, Y., Finkel, R.C., Caffee, M.W., Guoguan, Z. and Zhiqin, X., 2002.
923 Uniform postglacial slip-rate along the central 600 km of the Kunlun Fault (Tibet),
924 from 26Al, 10Be, and 14C dating of riser offsets, and climatic origin of the
925 regional morphology. Geophysical Journal International, 148(3), pp.356-388.

926 Van der Woerd, J., Y. Klinger, K. Sieh, P. Tapponnier, F.J. Ryerson, A.-S. Mériaux,
927 2006. Long-term slip rate of the southern San Andreas Fault from 10Be-26Al
928 surface exposure dating of an offset alluvial fan, Journal of Geophysical Research,
929 111, B04407, doi:10.1029/2004JB003559.
930 Wallace, K., Yin, G., and Bilham, R., 2004, Inescapable slow slip on the Altyn Tagh
931 fault: Geophysical Research Letters, v. 31, L09613, doi: 10.1029/2004GL019724.
932 Weldon, R. J., and K. E. Sieh. 1985. Holocene rate of slip and tentative recurrence
933 interval for large earthquakes on the San-Andreas Fault, Cajon-Pass,
934 Southern-California, Geol. Soc. Am. Bull., 96, 793-812.
935 Wells, D., and K. Coppersmith, 1994. New empirical relationships among magnitude,
936 rupture length, rupture width, rupture area, and surface displacement. Bull.
937 Seismol. Soc. Am. 84(4), 974–1002.
938 Xiang Hongfa, Guo Shunmin, Zhang Bingliang, Zhang Wanxia, Yasutaka Ikeda, He
939 Honglin, 1998. Active features of the eastern Liupanshan piedmont reverse fault
940 zone since late Quaternary. Seismology and Geology. 20(4): 321-327(in Chinese).
941 Xu, X., Wang, F., Zheng, R., Chen, W., Ma, W., Yu, G., Chen, G., Tapponnier, P.,
942 Van Der Woerd, J., Meriaux, A.S. and Ryerson, F.J., 2005. Late Quaternary
943 sinistral slip rate along the Altyn Tagh fault and its structural transformation model.
944 Science in China Series D: Earth Sciences, 48(3), p.384.
945 Yao Wenqian, Jing Liu-Zeng, M.E. Oskin, Wei Wang, Zhanfei Li, Veronica Prush,
946 Jinyu Zhang, Maoyun Tang, Yanxiu Shao, Zhaode Yuan, Longfei Han, Yann
947 Klinger. 2019. Re-evaluation of the Late Pleistocene slip rate of the Haiyuan fault
948 near Songshan, Gansu province, China. Journal of Geophysical Research: Solid
949 Earth, 124(5):5217-40.
950 Yuan Daoyang, Liu Baichi, Lv Taiyi, He Wengui, Liu Xiaofeng. 1997.
951 Palaeoearthquake features along the eastern segment of north Qilianshan active
952 fault zone. South China Journal of Seismology, 17(2): 24-31 (in Chinese).

953 Yuan Daoyang, Liu Baichi, Lu Taiyi, He Wengui, Liu Xiaofeng, and Gan Weijun,
954 1998. Study on the sectionation of the eastern section of north Qilianshan active
955 fault zone. Northwestern Seismological Journal. 20(4):27-34(in Chinese).
956 Yuan Daoyang, Zhang Peizhen, Liu XingWang, Ge WeiPeng, Molnar P., Zheng
957 WenJun, Zhang HuiPing, Liang MingJian, 2008. Late Quaternary strike-slip
958 features along the Halahua fault, western section of Haiyuan-Qilianshan fault, NE
959 Tibetan Plateau. AGU meeting, San Francisco, U.S.A.
960 Yuan, D.Y., Ge, W.P., Chen, Z.W., Li, C.Y., Wang, Z.C., Zhang, H.P., Zhang, P.Z.,
961 Zheng, D.W., Zheng, W.J., Craddock, W.H. and Dayem, K.E., 2013. The growth
962 of northeastern Tibet and its relevance to large-scale continental geodynamics: A
963 review of recent studies. Tectonics, 32(5), pp.1358-1370.
964 Zhang P., Molnar, P., Burchfiel, B. C., Royden, L., Wang, Y., Deng, Q., Song, F.,
965 Zhang, W., and Jiao D., 1988a. Bounds on the Holocene slip rate along the
966 Haiyuan fault, north-central China. Quat. Res. 30: 151–164.
967 Zhang P., Molnar, P., Weigi, Z., Qidong, D., Yipeng, W., Burchfiel, B.C., Fangmin,
968 S., Royden, L. and Decheng, J., 1988b. Bounds on the average recurrence interval
969 of major earthquakes along the Haiyuan fault in north-central China. Seismological
970 Research Letters, 59(3), 81-89.
971 Zhang, P., W. Min, Q. Deng, and F. Mao. 2003. Paleoearthquake rupture behavior
972 and recurrence of great earthquakes along the Haiyuan Fault, northwestern China,
973 Sci. China, Ser. D, 46, 705–713.
974 Zhang, P. Z., P. Molnar, and X. Xu, 2007. Late Quaternary and present-day rates of
975 slip along the Altyn Tagh Fault, northern margin of the Tibetan Plateau. Tectonics.
976 26, TC5010, doi:10.1029/2006TC002014.
977 Zhang, Y.P., Zheng, W.J., Zhang, D.L., Zhang, P.Z., Yuan, D.Y., Tian, Q.Y., Zhang,
978 B.X. and Liang, S.M., 2019. Late Pleistocene left-lateral slip rates of the Gulang
979 Fault and its tectonic implications in eastern Qilian Shan (NE Tibetan Plateau),
980 China. Tectonophysics. 756:97-111. Doi: 10.1016/j.tecto.2019.02.013.

981 Zheng, D. W., P. Z. Zhang, J. L. Wan, D. Y. Yuan, C. Y. Li, G. M. Yin, G. L. Zhang,
982 Z. C. Wang, M. Min, and J. Chen. 2006. Rapid exhuma- tion at similar to 8 Ma on
983 the Liupan Shan thrust fault from apatite fission-track thermochronology:
984 Implications for growth of the north- eastern Tibetan Plateau margin, Earth Planet.
985 Sci. Lett., 248(1–2), 198–208.
986 Zheng, W.J., Zhang, P.Z., He, W.G., Yuan, D.Y., Shao, Y.X., Zheng, D.W., Ge, W.P.
987 and Min, W., 2013. Transformation of displacement between strike-slip and crustal
988 shortening in the northern margin of the Tibetan Plateau: Evidence from decadal
989 GPS measurements and late Quaternary slip rates on faults. Tectonophysics. 584,
990 267-280.
991 Zielke, O., J R. Arrowsmith, L. B. Grant-Ludwig, and S. O. Akciz, 2010. Slip in the
992 1857 and earlier large earthquakes along the Carrizo section, San Andreas Fault.
993 Science. 327, 1119-1122, doi:10.1126/science.1182781.
994 Zielke, O., J R. Arrowsmith, L. B. Grant-Ludwig, and S. O. Akciz, 2012. High
995 resolution topography-derived offset along the 1857 Fort Tejon earthquake rupture
996 trace, San Andreas Fault. Bull. Seis. Soc. Am. 102(3), doi:10.1785/0120110230.
997 Zielke, O., Klinger, Y. and Arrowsmith, J.R., 2015. Fault slip and earthquake
998 recurrence along strike-slip faults—Contributions of high-resolution geomorphic
999 data. Tectonophysics. 638, 43-62.
1000 Zinke, R., Dolan, J.F., Van Dissen, R., Grenader, J.R., Rhodes, E.J., McGuire, C.P.,
1001 Langridge, R.M., Nicol, A. and Hatem, A.E., 2015. Evolution and progressive
1002 geomorphic manifestation of surface faulting: A comparison of the Wairau and
1003 Awatere faults, South Island, New Zealand. Geology. 43(11), 1019-1022.
1004
1005

Table 1. Radiocarbon dates table

Sample	Lab [a]	Depth (m)	Fraction Modern	±	$D^{14}C$ (‰)	±	^{14}C Age (B.P.)	±	2σ calibrated age (B.P.) [b]
HGD-C14-01	414950	0.77	0.4236	0.0016	-576.4	1.6	6900	30	Cal 7790 - 7675
HGD-C14-02	414951	0.62	0.4414	0.0016	-558.6	1.6	6570	30	Cal 7555 - 7545

a: All sample were AMS dated at Beta Analytic; b: Calibration with Calib 7.1 (Stuiver et al., 1998), did not include probability distribution of range < 0.1.

Table 2. Quartz OSL ages on T3

Sample No	Lab. no[a]	Depth(m)	Water content[b] (%)	U(ppm)	Th(ppm)	K(%)	Cosmic dose rate(Gy/ka)	grain size (μm)	Dose rate [c] (Gy/ka)	Equivalent dose[d] (Gy)	Age[e] (ka)
HGDOSL-1502	15-64	0.82	2.6	2.71±0.1	14.4±0.39	2.18±0.06	0.32±0.02	90-125	4.06±0.15	35.3±1.3	8.7±0.5
HGDOSL-1501	15-63	1.04	8.04	2.45±0.1	12.8±0.36	2.12±0.06	0.31±0.02	90-125	3.61±0.13	44.2±0.8	12.2±0.5

a: All samples were processed at Zhejiang Zhongke Institute of Luminescence Testing Technology;

b: The measured water content;

c: The concentrations of U, Th and K were measured by neutron activation analysis at the China institute of atomic energy;

d: All De values conform to normal distribution;

e: All De values were calculated by the central age model (Galbraith et al., 2012).

Table 3. Analytical data of ^{10}Be at Daqing site on the Haiyuan fault

Samples	Mass quartz (g)	Be Carrier (mg)	Latitude (N)	Longitude (E)	Altitude (m)	Depth (cm)	Thickness (cm)	Sample type	10Be/9Be	10Be/9Be error (%)	10Be ± error (atom/g)	Exposure age ± uncert (yr)
T1 surface												
HGD14-08	30.107	0.2461	37.259544	102.696663	3441	0	2.5	boulders	1.11247E-12	3.1680	608254 ± 19269	13344 ± 1205
HGD14-09	26.9599	0.2699	37.259254	102.696609	3432	0	2.5	boulders	5.23986E-13	3.0904	350879 ± 10843	7705 ± 693
HGD14-10	25.7075	0.241	37.259041	102.696503	3426	0	2.5	boulders	7.61713E-13	3.1744	477641 ± 15162	10529 ± 951
HGD14-16	30.0079	0.2458	37.256313	102.695001	3369	0	2.5	boulders	3.02524E-13	3.1761	165752 ± 5264	3956 ± 357
HGD14-22	29.8354	0.25	37.256969	102.695702	3389	0	2.5	boulders	6.77539E-13	3.1746	379748 ± 12055	8594 ± 776
HGD14-23	29.972	0.2517	37.257381	102.695984	3393	0	2.5	boulders	8.62754E-14	3.5217	48462 ± 1706	1165 ± 106
T2 surface												
HGD14-18	30.0132	0.2901	37.255253	102.694336	3351	0	2.5	boulders	1.11507E-12	3.0821	720924 ± 22219	16489 ± 1486
HGD14-19	24.5073	0.2253	33.255444	102.69445	3354	0	2.5	boulders	1.41835E-12	3.4983	872173 ± 30511	21606 ± 1982
HGD14-20	30.0075	0.2495	2m south of 19			0	2.5	boulders	2.79689E-12	1.9939	1555499 ± 31016	36437 ± 3185
HGD14-25	30.0081	0.2555	37.256226	102.694389	3371	0	2.5	boulders	1.37277E-12	3.0506	781814 ± 23850	17590 ± 1584
HGD14-26	25.0845	0.2432	37.257112	102.69458	3388	0	2.5	boulders	1.23744E-12	3.0546	802483 ± 24512	17877 ± 1610
HGD14-27	30.0488	0.2546	37.257439	102.694618	3391	0	2.5	boulders	9.21578E-13	3.1078	522297 ± 16232	11788 ± 1062
HGD14-28	30.0016	0.253	37.257252	102.69455	3393	0	2.5	boulders	1.12670E-12	3.1186	635531 ± 19820	14360 ± 1295
T3 depth profile												
HGDT3-01	31.4296	0.2592	37.257061	102.693886	3389	85	5	gravel	1.30104E-12	2.4296	717695 ± 17436	See model
HGDT3-02	29.9764	0.2484	37.257061	102.693886	3389	100	5	gravel	2.05011E-12	2.6603	1136327 ± 30229	/

HGDT3-03	25.1784	0.2563	37.257061	102.693886	3389	115	5	gravel	8.73919E-13	3.1803	595039 ± 18923	/
HGDT3-04	32.0859	0.2514	37.257061	102.693886	3389	145	5	gravel	7.71630E-13	3.2954	404402 ± 13326	/
HGDT3-05	30.1135	0.2566	37.257061	102.693886	3389	175	5	gravel	5.80584E-13	3.0688	330913 ± 10154	/
HGDT3-06	29.3054	0.254	37.257061	102.693886	3389	205	5	gravel	6.24376E-13	3.0946	361981 ± 11201	/
HGDT3-07	30.0178	0.2501	37.257061	102.693886	3389	245	5	gravel	6.97878E-13	3.5702	388926 ± 13885	/
HGDT3-08	30.041	0.2549	37.257061	102.693886	3389	285	5	gravel	4.62999E-13	3.2264	262778 ± 8478	/

Note: All samples were taken chemical process at the Key Laboratory of Crustal Dynamics, China Earthquake Administration and AMS measurement at Centre de Recherche et d'Enseignement de Géosciences de l'Environnement (CEREGE) of France. Scaling scheme for spallation: Time-dependent Lal (1991) / Stone (2000), ages calculated with the CRONUS 2.3 calculator (http://hess.ess.washington.edu/), density of sample is assigned simply with 2.7 g/cm^3 , erosion rate is zero.

Table 4. Terrace displacement and geometry measurement

	Marker	Parameter	Value/m	error/m	Note
Horizontal Offset	Stream	Ds	6.0	0.5	
	T2/T1	D2u	35	2	
		D2l	27	2	
		d2u	6.5	1	
		d2l	6.5	1	
	T3/T2	D3u	94	3	
			82	3	
		D3l	72	3	
		d3u	25	2	
		d3l	28	2	
	T2’	D2’	29	2	
		West bank	28	2	
Vertical offset	T1 tread interior	Sc1	1.3	0.2	
	T2’ interior		5.7	1	
	T2’ outer		6.4	1	
	T2 tread interior	Sc2	9	1	
	T2 tread outer		10	1	
	T3 tread interior	Sc3	19	2	
	T3 tread outer		15	2	
Width	T1 tread	W1u	61	4	upstream
	T1 tread	W1l	34	2	downstream
	T2’		42	2	upstream
	T2’		42	2	downstream
	T2 tread	W2u	135	5	upstream
	T2 tread	W2l	89	3	downstream
Height	T1-T0 tread	R1u	6	1	upstream
		R1d	2.5	0.5	downstream
	T2-T1 tread	R2u	16-17	1	There is a bump at upstream of T2 tread
		R2d	7.5	1	downstream
	T3-T2 tread	R3u	10-15	1	There is a bump at upstream of T2 tread
		R3d	1.4-1.7	0.3	downstream

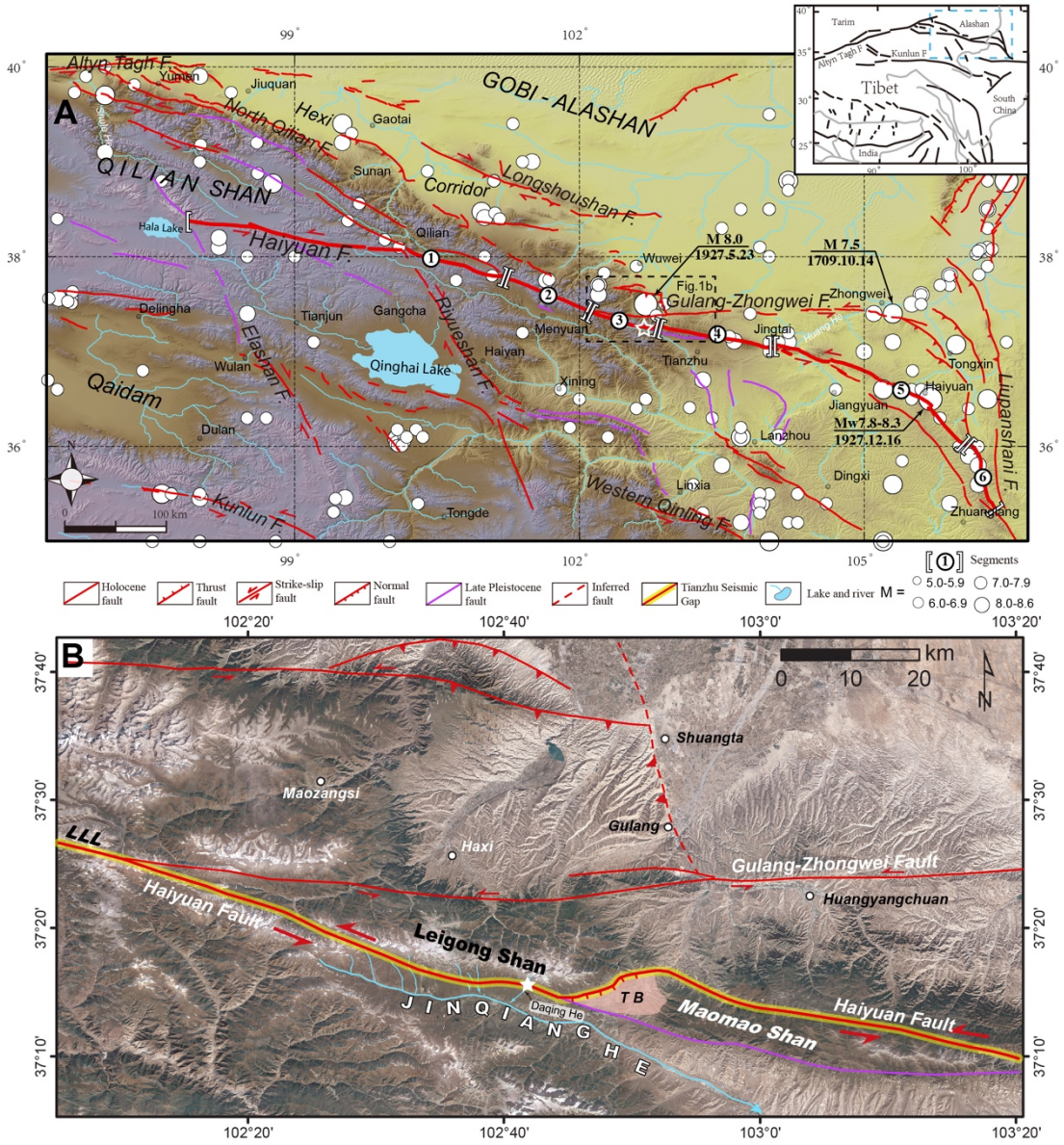

Figure 1. (A) Active faults map of northeastern Tibetan Plateau. Seismicity from B.C. 780 to A.D. 2006, Historical earthquake from Division of Earthquake Monitoring and Prediction, State Seismologic Bureau (1995), instrumental seismicity from China Earthquake Networks Center (http://www.cenc.ac.cn/). White star indicates study site, dashed box is figure 1B. Haiyuan fault is subdivided into six sections (1): Halahu, (2): Lenglongling, (3): Jinqiang He, (4): Maomao Shan, (5): Haiyuan, (6): Liupan Shan. Inset is location of map in tectonic frame of Tibetan Plateau. (B) Active faults along Jinqiang He section that extends from Lenglongling-Gulang-Jinqiang (LGH) faults triple junction to the west, to Tianzhu pull-apart basin (TB) to the east, left-stepping to Maomao Shan section. Jinqiang He Valley is fed mostly by north-south tributaries that are cut by Haiyuan fault and flowing down from Leigong Shan. LLL: Lenglongling.

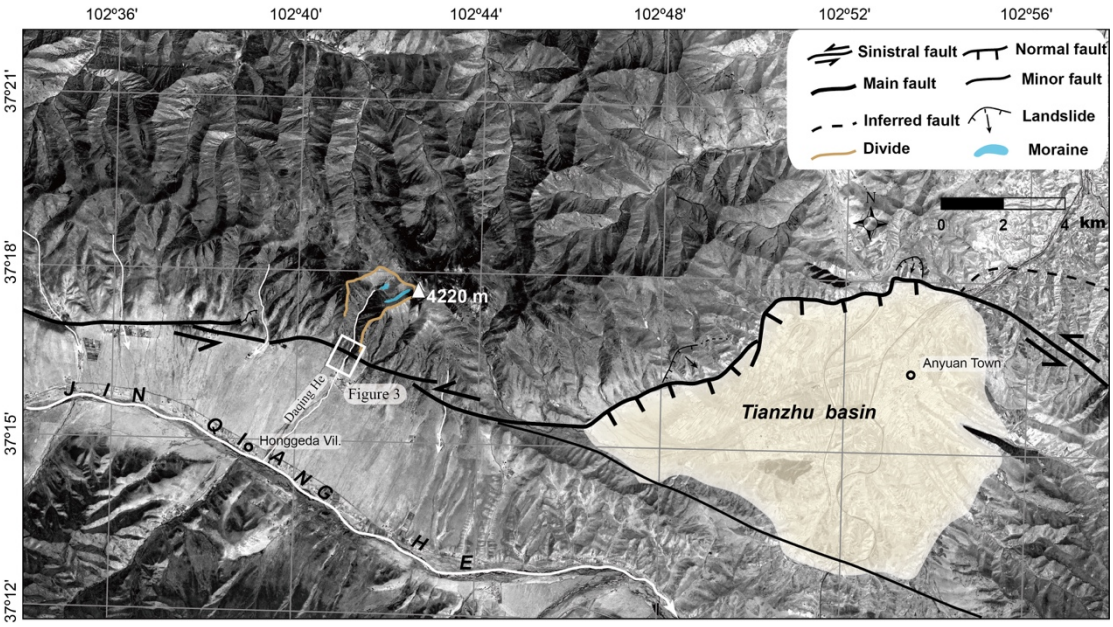

Figure 2. GF-1 satellite imagery (pixel ~2m) of Haiyuan fault near Daqing site (white rectangle) upstream from Honggeda village. Light shading delimits Tianzhu basin.

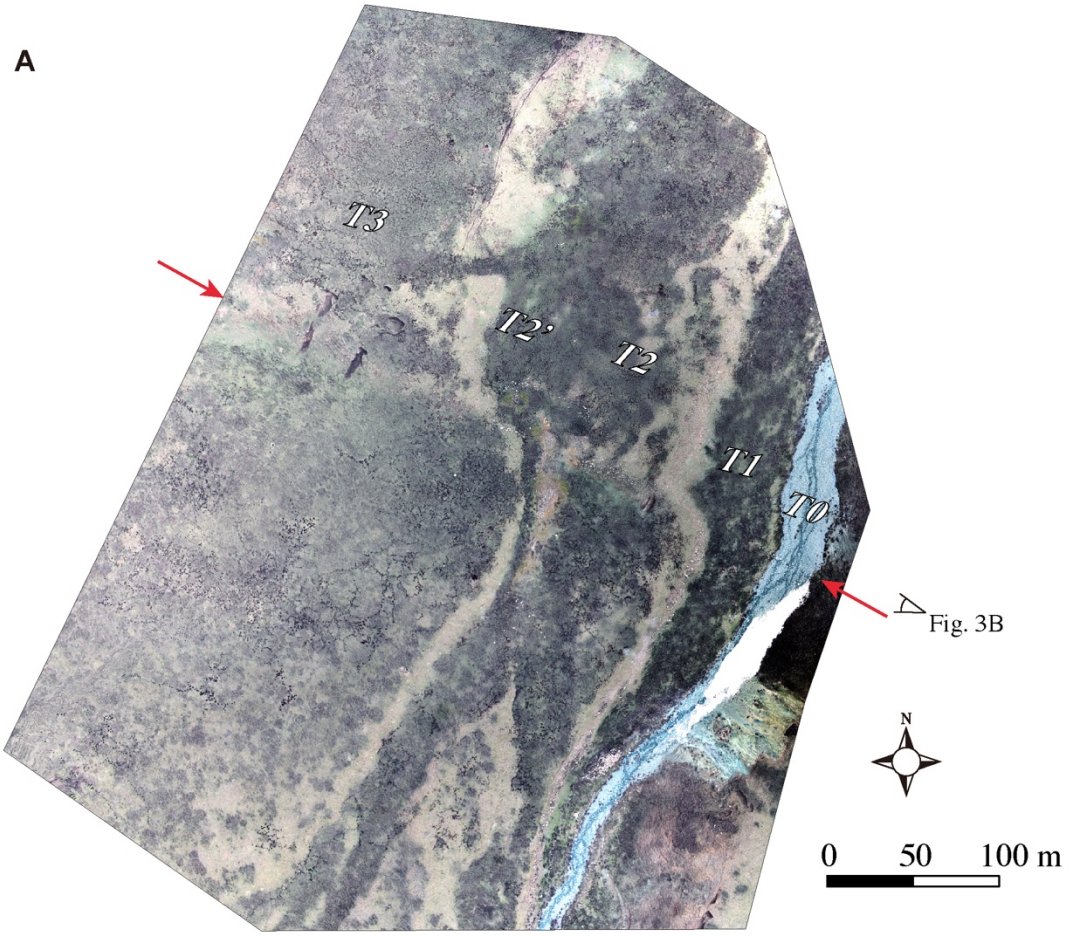

Figure 3. (A) Unmanned aerial vehicle (UAV) derived photo mosaic with ~0.2m resolution. Fault trace is clear across stream bed T0 and terraces T1 to T3 west of it. Red arrows point to the fault trace. (B) West looking panoramic field view of faulted terraces at Daqing site.

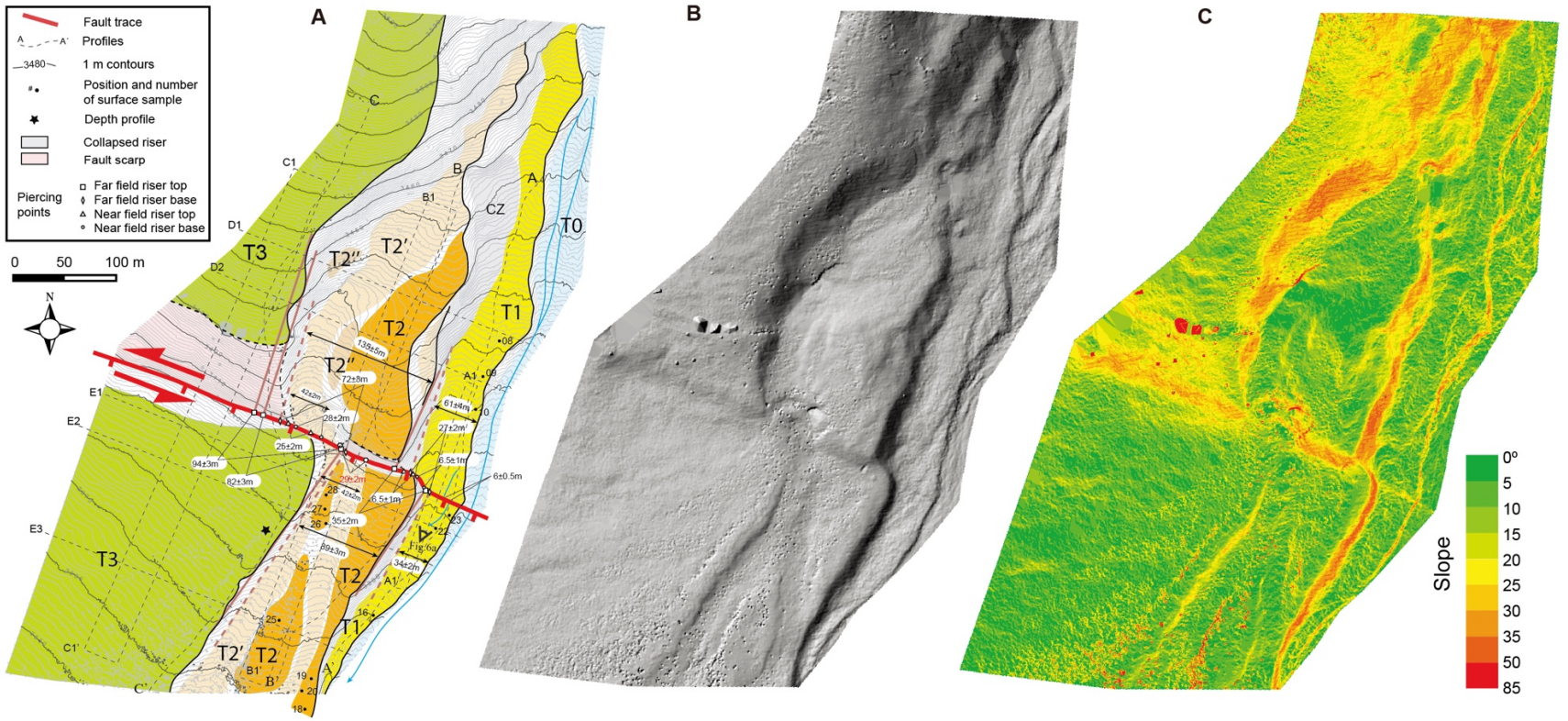

Figure 4. (A) Geomorphic map of Daqing site. Contours with 1 m interval derived from ~0.1m resolution DEM from terrestrial LiDAR. Field topographic profiles levelled with Trimble RTK, dashed rectangles and lines are swath and cross profiles extracted from DEM (see figure 7).

Surface sample numbers abbreviated without prefix “HGD14-”. Purple lines are piercing lines for horizontal slip measurement. (B) Hill shading and (C) slope map of DEM highlighting terrace surface morphology, distinct terrace risers and fault scarp.

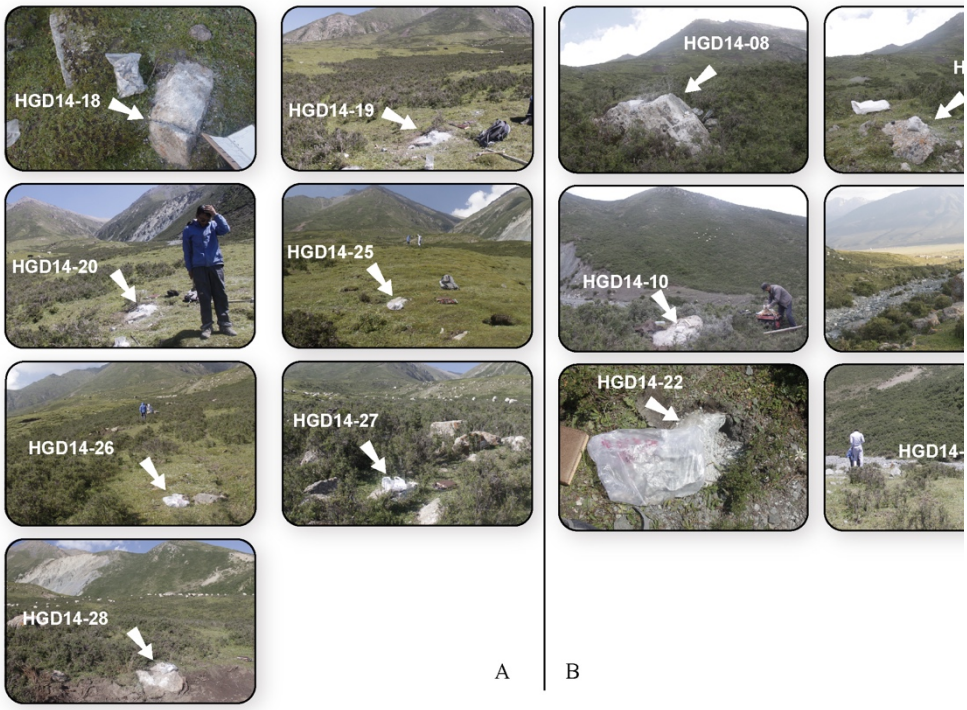

Figure 5. Field photographs of surface samples for cosmogenic dating with s
numbers on T2 (A) and T1 (B). White arrows point to boulders where sampl
from.

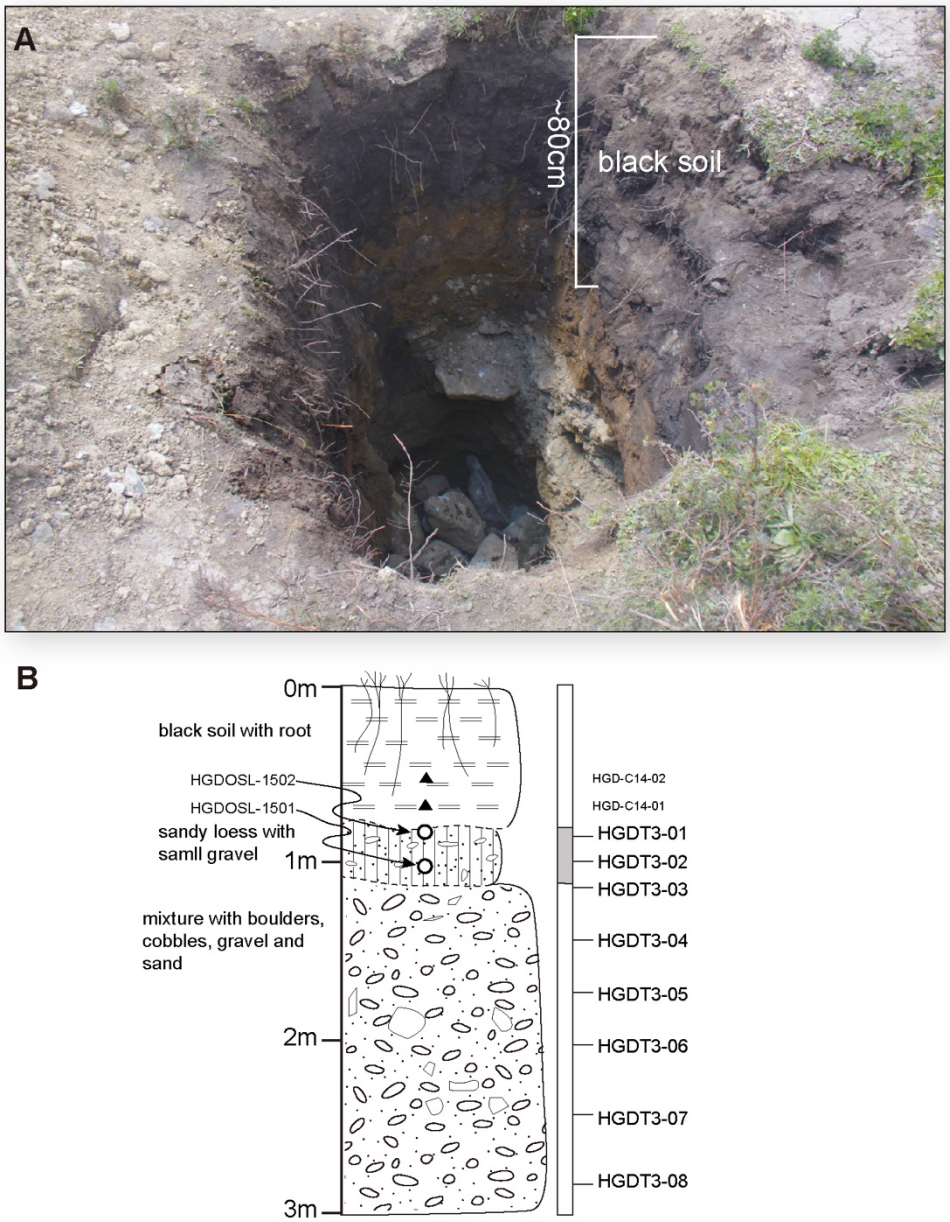

Figure 6. (A) Sampling pit on T3. (B) Stratigraphic description of pit. Eight sand and gravel samples were collected from below ~80 cm to ~3 m depth for cosmogenic isotope dating. Open circles are sandy loess samples for OSL dating, solid triangles are black soil samples for ^{14}C dating.

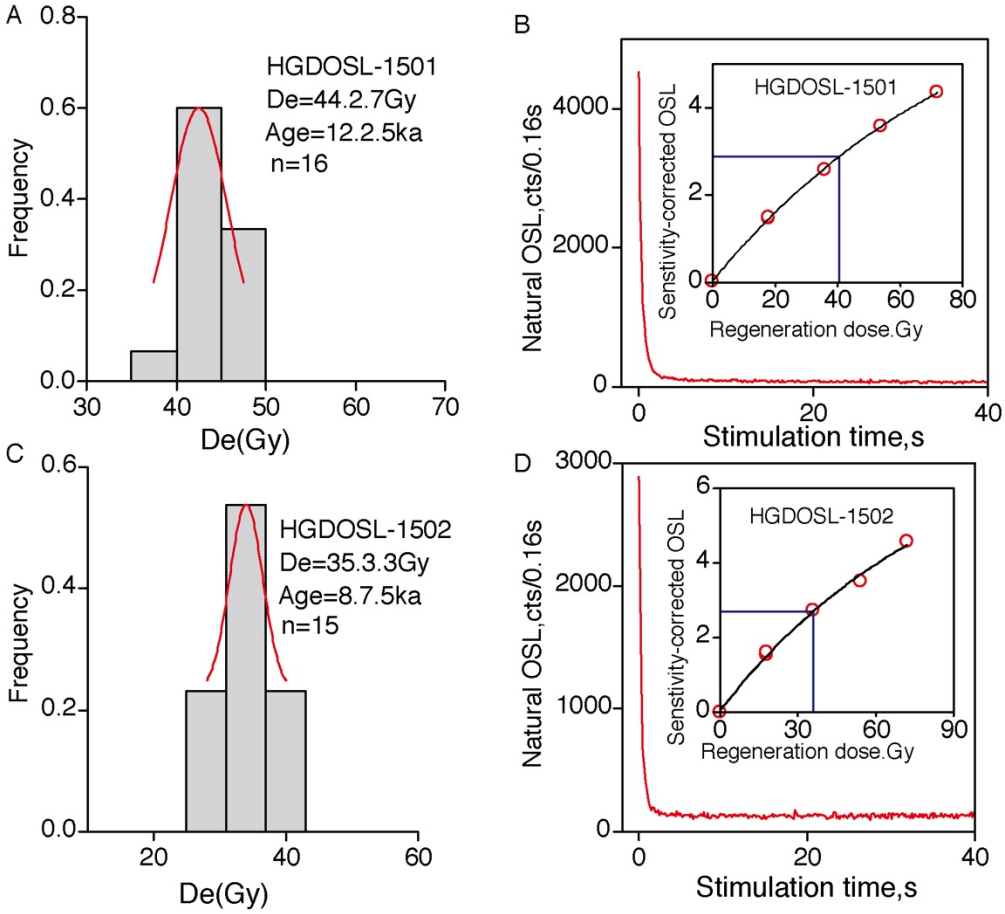

Figure 7. The De distributions, natural OSL decay curve and growth curves for samples HGDOSL-1501 (A and B) and HGDOSL-1502 (C and D).

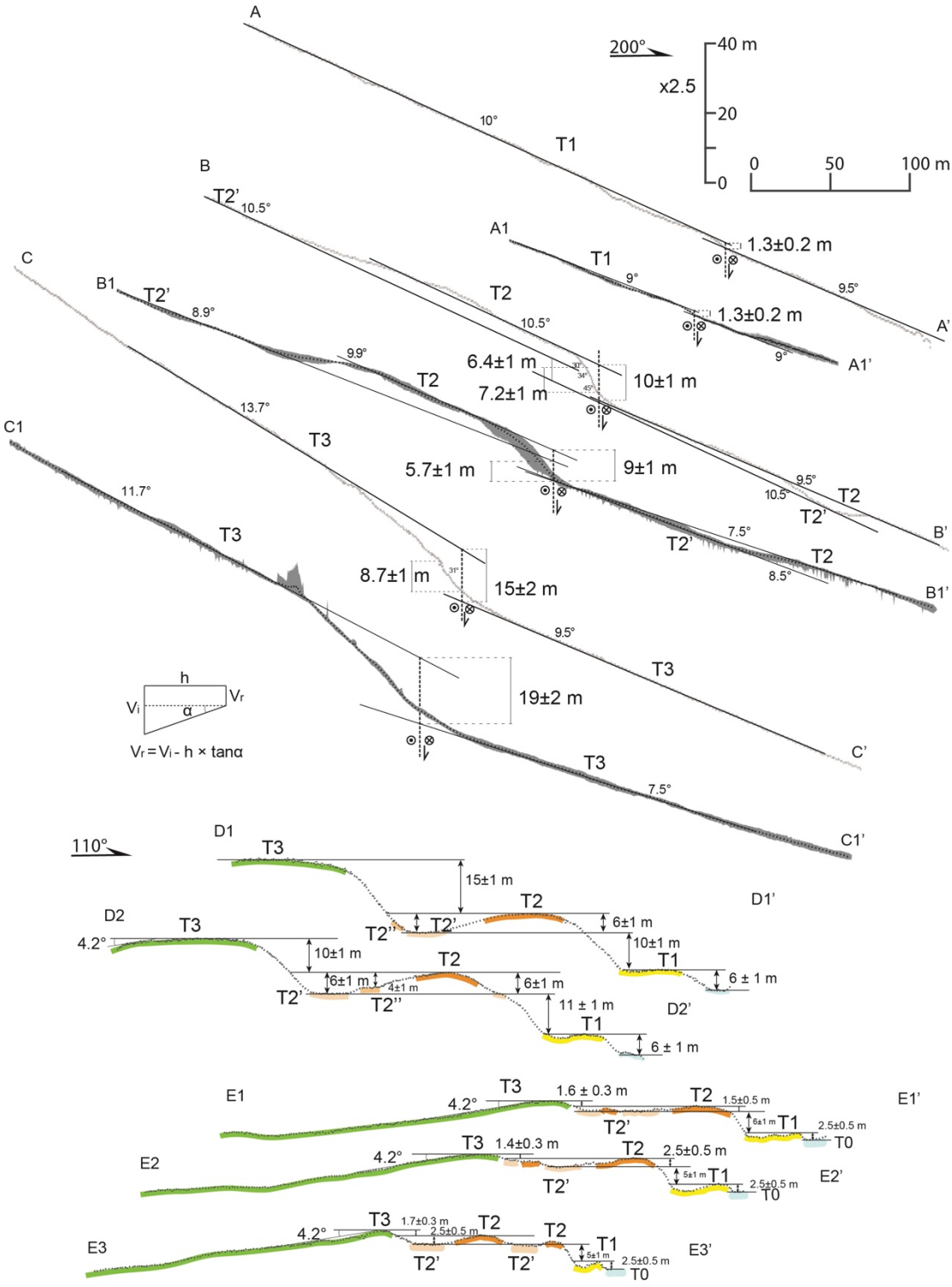

Figure 8. Topographic profiles across terraces at Daqing site. Locations shown in Figure 4. Gray dots are measurement points, solid black lines along slopes are fitting lines. AA', BB' and CC' are GPS-RTK profiles, swath profiles extracted from LiDAR-DEM. Dashed line in swath profile represents mean elevation value. Small sketch illustrates correction applied to apparent vertical offset of T3 due to oblique

offset of sloping surface. Vr, corrected vertical offset, is function of Vi vertical throw measurement from perpendicular to fault profile C1-C1', h is horizontal offset of terrace, α is angle between maximum slope direction and perpendicular to fault (about 4.2°) (see also Gaudemer et al., 1995).

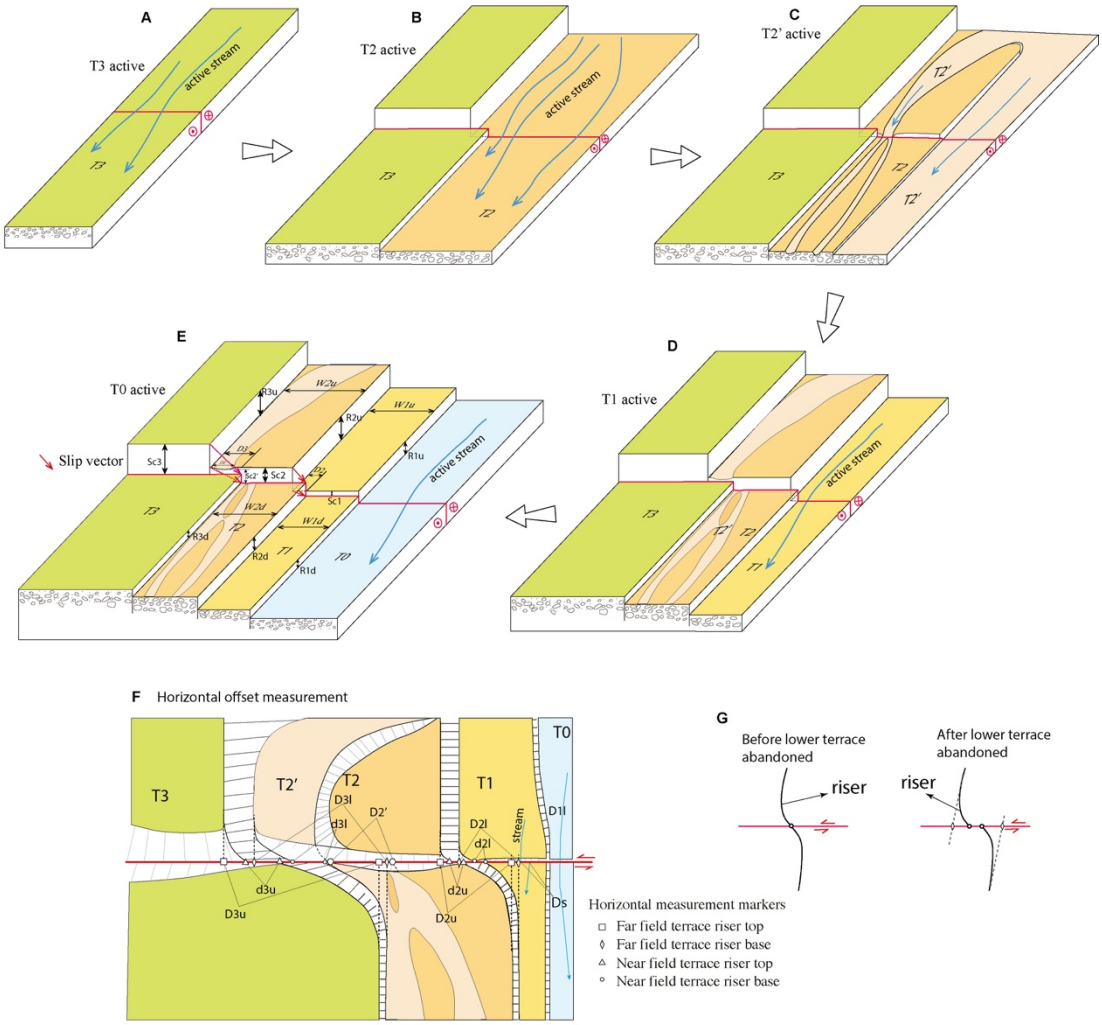

Figure 9. Offset terraces reconstruction. (A)-(E) are diagrams of different stages during river downcutting, lateral erosion and displacement accumulation. Simplified risers are vertical. (F) sketch of offset terraces at our Daqing site. All measurement results are shown in Table 4. (G) shows how near field (d3u, d3l, d2u and d2l) and far field displacements are related.

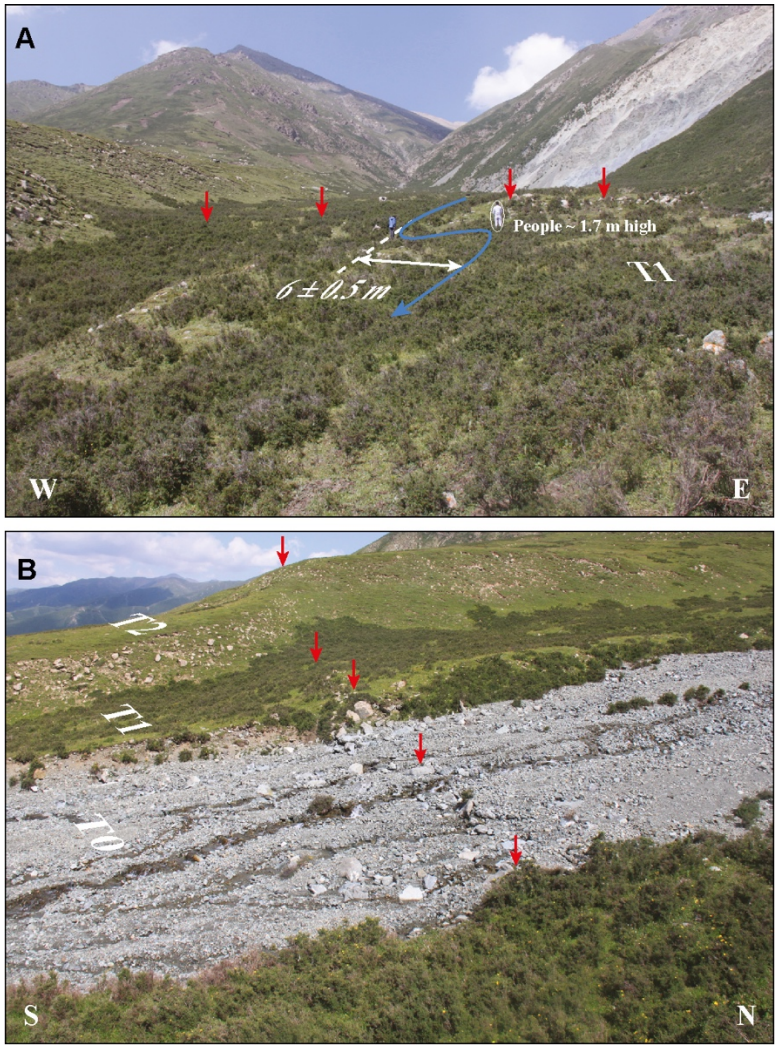

Figure 10. Field details of fault trace at Daqing site. (A) Small stream offset on terrace T1. Red arrows indicate top of fault scarp across T1. (B) Oblique view showing fault trace across T0, T1 and T2.

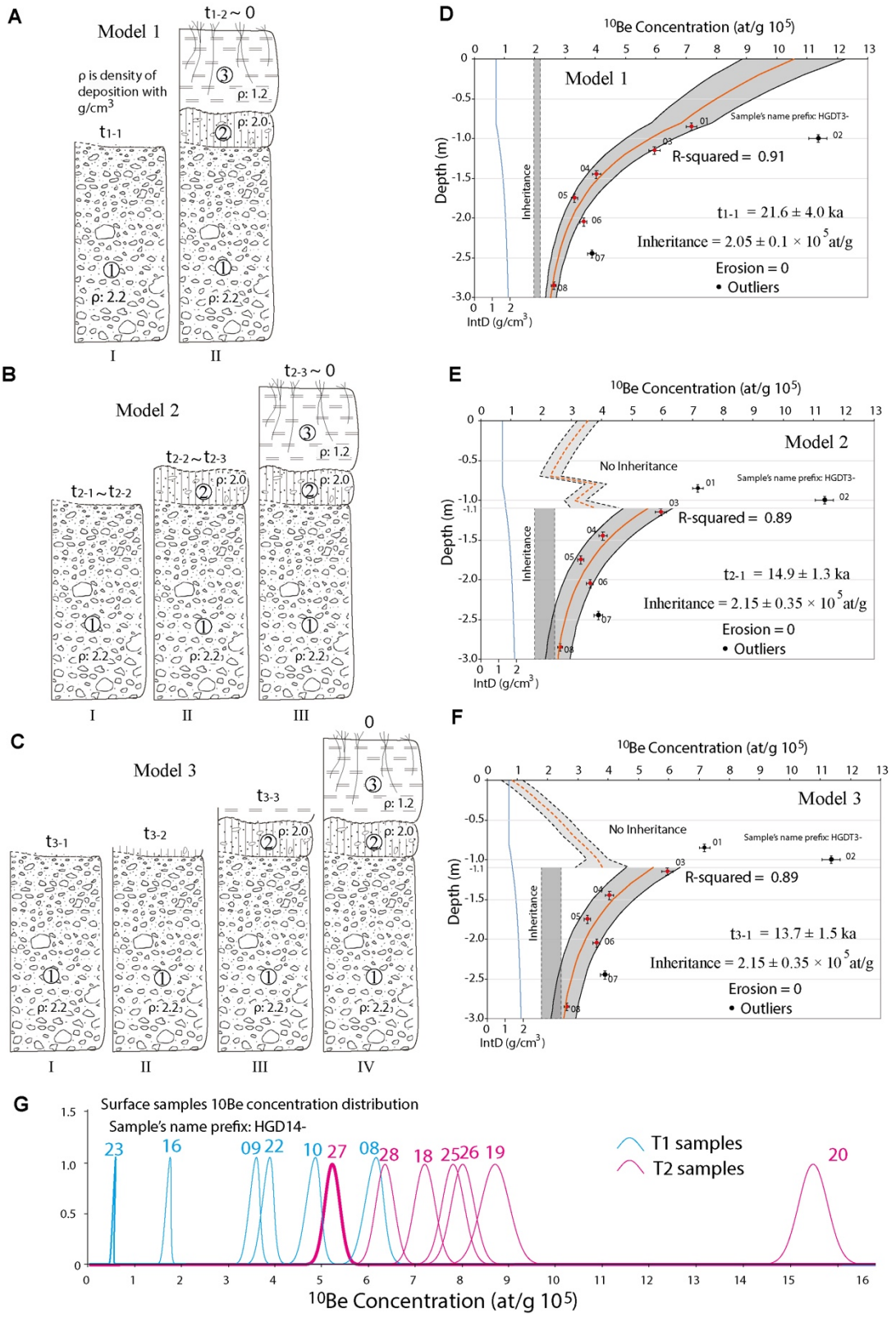

Figure 11. Exposure age constraints at Daqing site. (A), (B) and (C) are proposed end-member models of T3 depth profile. $t_{1\text{-}1}$, $t_{2\text{-}1}$and $t_{3\text{-}1}$ are abandonment ages. (A and D) model 1: loess and soil are deposited immediately after T3 conglomerate, $t_{1\text{-}1}$ equals to $t_{1\text{-}2}$. Maximum age is 21.6 ka ($t_{1\text{-}1}$) with R-squared of 0.91. (B and E) model 2: three exposure stages: conglomerate without shielding ($t_{2\text{-}1}$ -$t_{2\text{-}2}$), sandy-loess

shielding ($t_{2\text{-}2}$ -$t_{2\text{-}3}$), and soil shielding ($t_{2\text{-}3}$ -0) in (B). Sandy-loess and soil are instantaneous deposits. Exposure age of 14.9 ka ($t_{2\text{-}1}$) with R-squared of 0.89. (C and F) model 3: progressive deposition of upper sandy-loess and soil layers. Model gives minimum age of 13.7 ka with R-squared of 0.89. Black circles are outliers not considered in modeling. More realistic model 3 takes into account OSL and 14C dates. $t_{2\text{-}2}$, $t_{2\text{-}3}$, $t_{3\text{-}2}$, and $t_{3\text{-}3}$ are constrained by dates of sandy-loess and soil. (G) ^{10}Be concentrations of surface samples of T1 and T2.

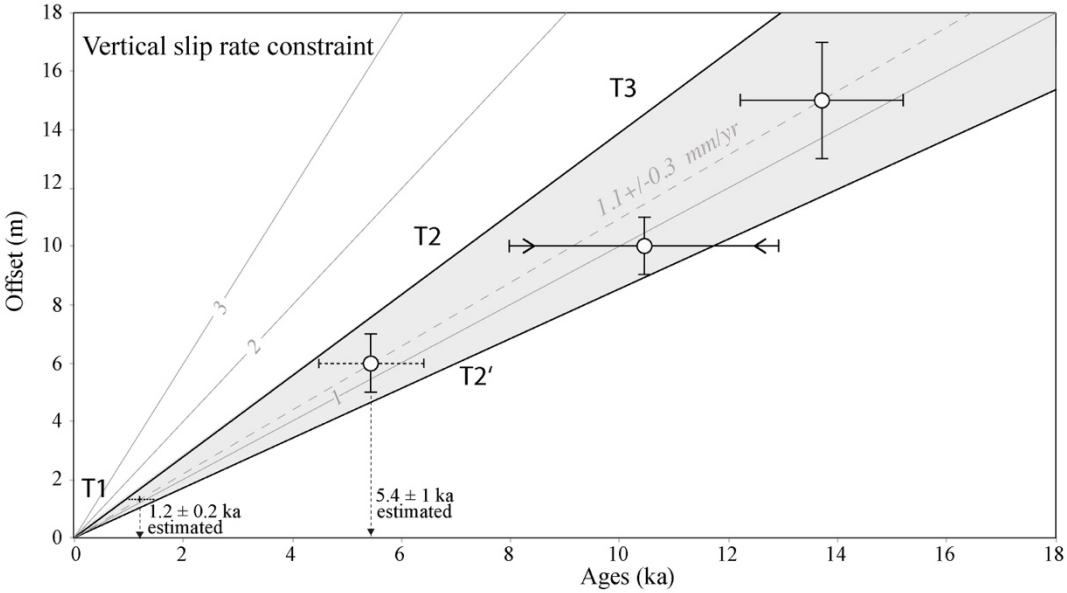

Figure 12. Vertical slip rate determination based on data from T3 and T2 at Daqing site on the Haiyuan fault. Oblique lines are slip rates in mm/yr. Gray shaded area is preferred range of slip value with a mean of 1.1 mm/yr. Combining this mean vertical slip rate and the vertical offsets of T2' and T1, their ages are estimated at 5.4 ka and 1.2 ka, respectively.

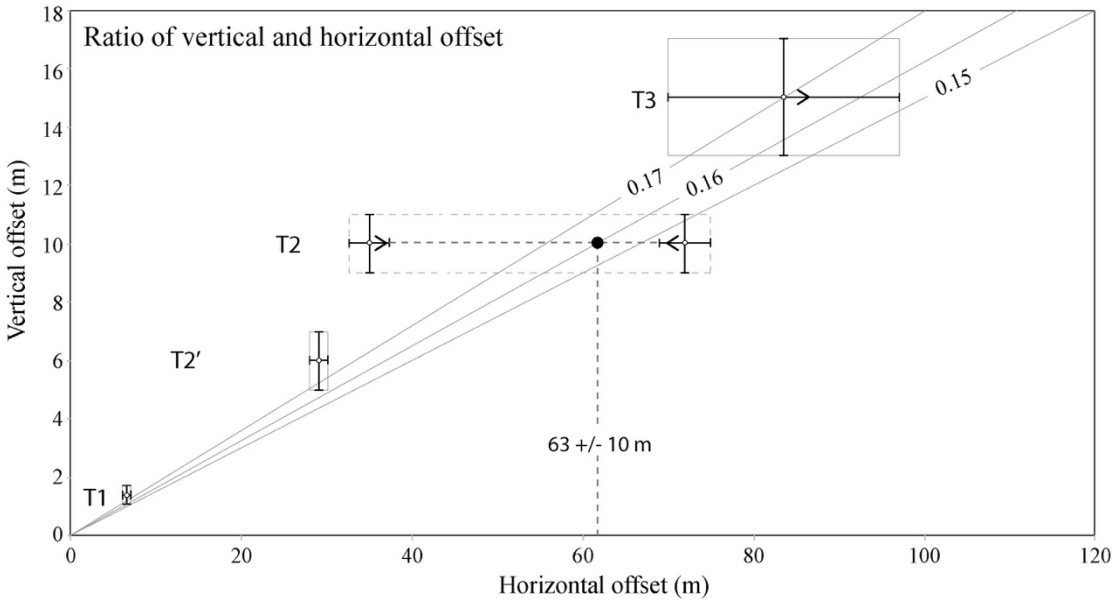

Figure 13. Ratio of vertical to horizontal offsets. T3 with a minimum horizontal offset. Best estimated ration is 0.16+/-0.01 by T3, T2' and T1. Because of, lateral erosion and river bed incision, vertical offset may accumulate earlier than the horizontal displacement of lower risers. Total horizontal offset of T2 might be estimated at 63 m based on average ratio.

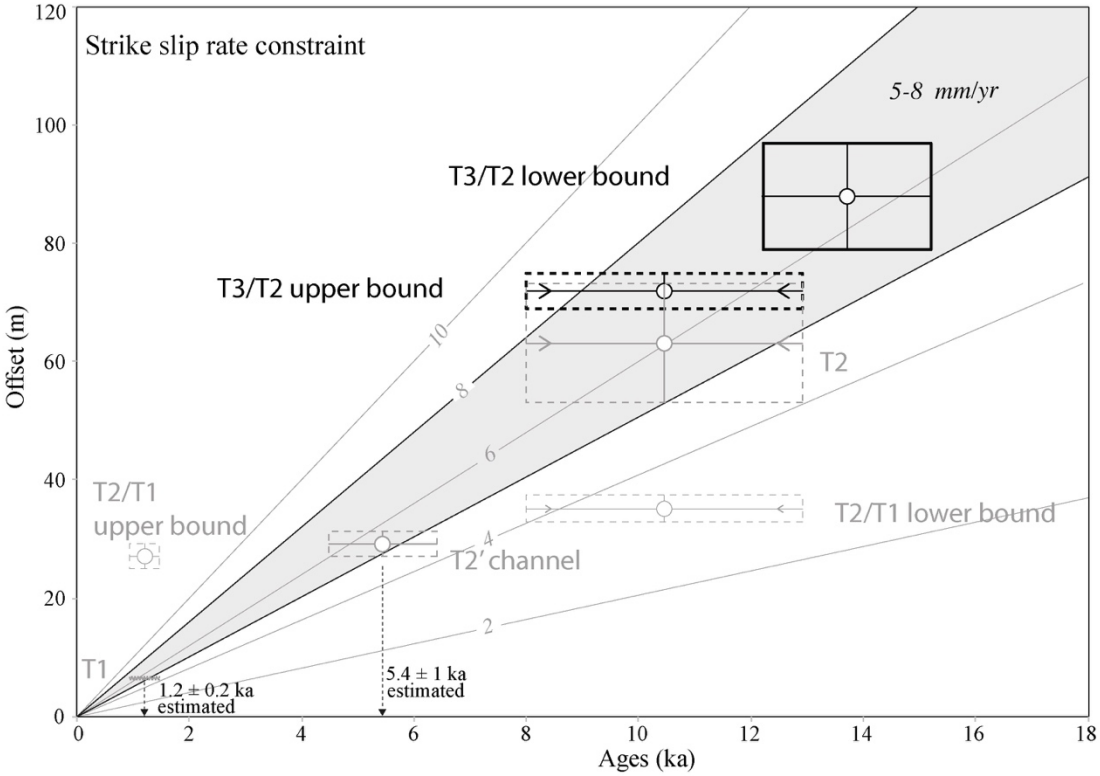

Figure 14. Strike slip rate determination at Daqing site. Oblique lines are slip rates contour with unit in mm/yr. Dashed rectangles represent weak data envelopes, but Solid rectangle is best determined rate, dashed rectangles are based on estimated data. Gray shaded area is preferred range of rates of between 5 and 8 mm/yr.